NANOMATERIALS:

FROM INTERFACIAL CHARACTERISTICS TO DEVICE APPLICATIONS

Doctor of Philosophy (2011) McMaster University

(Department of Materials Science & Engineering) Hamilton, Ontario

TITLE: Nanomaterials: from Interfacial Characteristics to Device Applications

AUTHOR: Kewei Wang

SUPERVISORS: Prof. Dr. Gu Xu, Prof. Dr. Hany Aziz

and Dr. Richard A. Klenkler

NUMBER OF PAGES: XIV, 121

NANOMATERIALS:

FROM INTERFACIAL CHARACTERISTICS TO DEVICE APPLICATIONS

By

KEWEI WANG

A Thesis

Submitted to the School of Graduate Studies

in Partial Fulfillment of the Requirements

for the Degree

Doctor of Philosophy

McMaster University

Abstract

Nanomaterials have been heavily studied in the past two decades. Previous findings have demonstrated that the characteristics of nanocomposites and the performance of nanomaterial-based devices are both determined by the interfacial characteristics of the nanomaterials. However, there are still some remaining challenges from interfacial characteristics to device applications, which are specified as follows: the difficulty in identifying the interfacial contacts of nanostructured surfaces, the instability of nanocomposite surfaces, and the under-researched mechanism of the correlation between interfacial characteristics and the performance of devices.

Therefore, the main theme of this thesis is to investigate the interfacial contacts of nanostructured solid-liquid interfaces by direct observation, and to develop a stable nanocomposite based on which the direct observation of the interfacial contact can be better conducted, and to eventually investigate the effect of interfacial contacts on the performance of organic solar cells.

As the previous identification of the solid-liquid interface is limited to a microscale range, a direct method of tracing the different wetting states of water was developed, on nanostructured surfaces. This method provided an answer to a long standing question of, whether there is a transition from Wenzel to Cassie states in the sliding angle drop on nanocomposite thin films. In order to complete the observation of the wetting states of water, a stable superhydrophobic nanocomposite thin film with hierarchical structure was developed.

Furthermore, with the knowledge of identifying the wetting states and the preparing procedures of the nanocomposites, a surfactant-free small-molecule nanoparticle organic solar cell with a much improved fill factor was developed by spin coating. The inverse correlation of series resistance and parallel resistance was discovered, due to the morphology change and the variation of the charge carrier concentration near the donor-acceptor interface in small-molecule organic solar cells.

Acknowledgements

I would like to express my deepest gratitude to Dr. Gu Xu, my supervisor, who guided me through the whole process of my study with valuable ideas, insightful comments and continuous encouragement. His enthusiasm and integrity as a scholar will influence me well in future.

I am also extremely grateful to my co-supervisors, Dr. Richard Klenkler and Dr. Hany Aziz, for their patient guidance and for providing great opportunities to work at Xerox Research Centre of Canada, and University of Waterloo. Special thanks go to Dr. Tony Petric and Dr. Igor Zhitomirsky, for their constructive advice and useful discussions.

I wish to thank Dr. Yu Qi and Dr. Nan-Xing Hu for their helpful suggestion and criticism to my research work. I would also like to give my gratitude to Dr. Avery Yuen and Dr. Yiliang Wu for their help and support.

I would also like to extend thanks to my colleagues and friends for discussing scientific questions.

To my parents and my wife, Ting, I wish to give my most sincere gratitude for their guidance, patience and endless support to overcome any difficulty during this study.

To my parents and my wife, Ting, for their support and encouragement.

Table of Contents

List of Figures

List of Tables

Chapter 1 Introduction

1.1 Nanomaterials

Nanomaterials are of special interests to the materials-research community over the past decades, due to their potential applications in catalysts, biomedicines, and electronics. Probably unbeknownst to us, nanomaterials have become part of our everyday lives. For example, nanoparticles of metal oxide have been used in sun lotions to block ultraviolet lights and nanomaterial thin films have been applied in the central processing unit (CPU) of our computers, which have brought about real technological revolutions.

The research of nanomaterials focuses on the creation and exploitation of materials which have morphological characteristics from atoms to bulk materials, and with at least one dimension in the nanoscale range. Figure 1.1 shows the typical ranges of some materials.

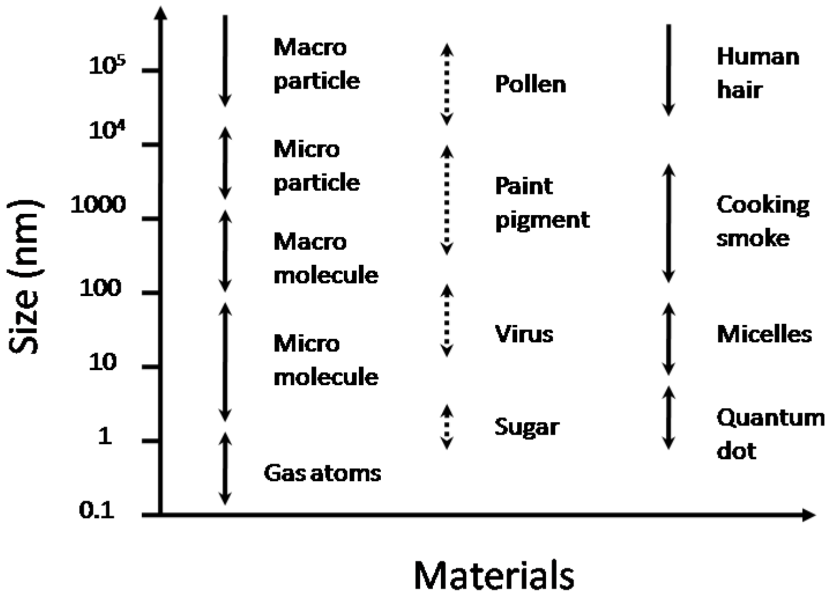

Figure 1.1: Typical ranges of some materials.

Nanomaterials are not a simple extension of miniaturization from microscale down to nanoscale. Microscale materials mostly exhibit the same physical properties as bulk materials. However, properties of nanomaterials are significantly different from those of bulk materials, such as the lower melting point, the enhanced mechanical strength, and the shift of absorption spectrum.

Therefore, the research on nanomaterials aims to obtain an in depth understanding of the new phenomena of nanomaterials, to further develop novel functional materials and to boost the invention of new devices. To achieve such goals, scientific areas such as physics, chemistry, materials science, and biology have been integrated in the course of enquiry. Figure 1.2 shows the scientific areas integrated in the research on nanomaterials as well as the main goals of such research.

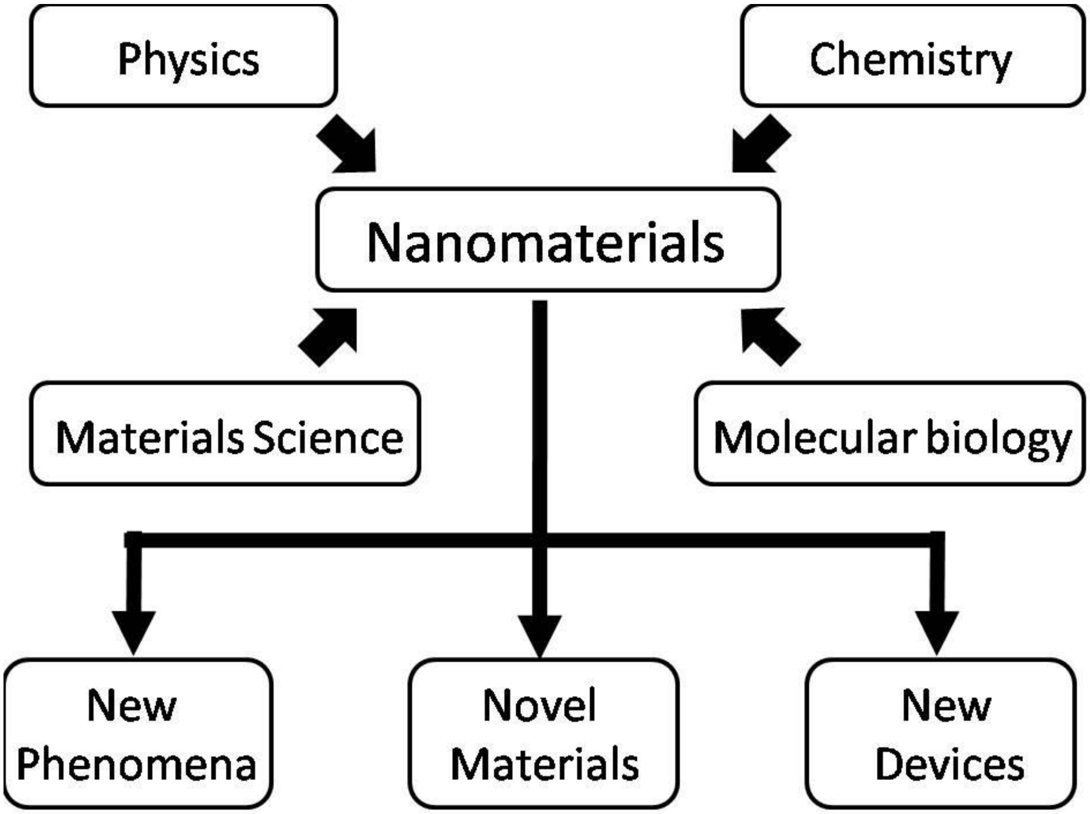

Figure 1.2: The scientific areas integrated in the research on nanomaterials and the main research goals.

The synthesis and characterization of nanomaterials and the fabrication of devices are two major research areas in nanomaterials.

As the starting point of research on nanomaterials, the synthesis and processing of nanomaterials provide various materials with different size, morphology, microstructure and chemical compositions. Based on this, the physical and chemical properties of these nanomaterials are further explored by the recent revolutionary instruments and approaches that allow the investigation with a resolution close to the atomic level. By utilizing these new properties, new nano-devices and devices with nanomaterials as building blocks are designed and fabricated, which will further lead to deeper understandings of the phenomena and to answers to some long standing questions. Finally, these new knowledge can help to accelerate the development of the synthesis, characterization and fabrication of devices.

1.2 From Interface Characteristics to Device Applications

Due to the small particle size, the surface area of the nanomaterials is much larger than that of bulk materials, leading to a large fraction of surface atoms, large surface energy and reduced imperfections. Moreover, the nanoparticles can be assembled into various nanostructures and microstructures. These features give unique electrical, chemical, optical, and mechanical properties to nanomaterials, which would inspire the creation and fabrication of new devices and the invention of new technologies.

Here is an example of how the interfacial characteristics affect the device applications. Nanomaterials have a significantly lower melting point than bulk materials, due to a large fraction of surface atoms in the total amount of atoms. For example, the melting point of bulk silver is as high as 1234K. However, it decreases rapidly to only 375K for silver nanoparticles with sizes below 5nm.[1] Because silver nanoparticles can be annealed under 100ºC to form silver lines, the silver nanoparticle dispersion can be used to print circuits onto plastics, films, and textiles, as shown in Figure 1.3.[2]

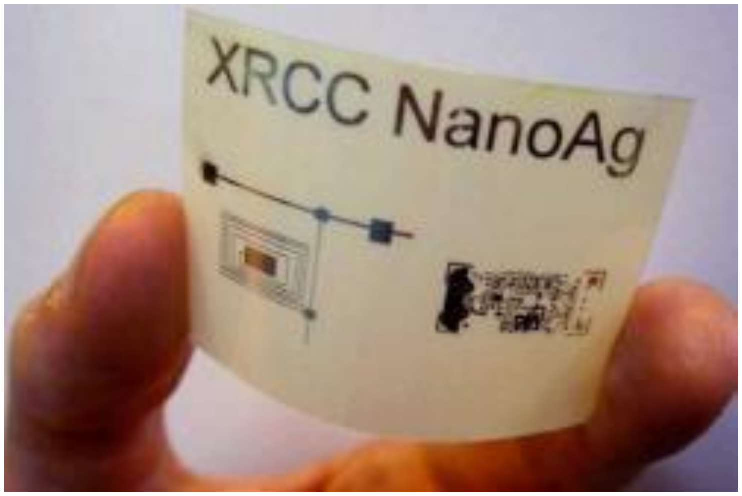

Figure 1.3: The fine lines printed by silver inks.

As introduced above, the interfacial characteristics of nanomaterials have a strong effect on the properties of nanomaterials, and as a result, they further influence the performance of the nanomaterial-based devices.

1.3 Challenges in Nanomaterial Systems and Devices

Nanomaterial-based systems and devices have attracted huge interests from the researchers over the past decades. Up to now, intensive research on the interfacial characteristics of nanomaterials has led us to a deeper understanding. However, some challenges still exist in the characterization, fabrication, and device application, e.g. the difficulty in identifying the interfacial contacts of nanostructured surfaces, the instability of nanocomposites with the complicated synthesis methods, and the under-researched mechanism of the correlation between interfacial characteristics and the performance of devices (e.g. organic solar cells).

The first challenge is the difficulty in identifying the interfacial contacts of nanostructured surfaces, especially the interfacial contacts of nanoscale surfaces in solid-liquid interface. To observe the solid-solid interface, microscope has been used to examine the crystal boundary for over decades. However, the microscope cannot be applied to study the nanoscale interface, due to the diffraction limit of visible light. Therefore, transmission electron microscopy (TEM) is applied to directly observe the solid-solid interface, e.g. interfaces between carbon nanotubes and polymers.[3]

However, because of the vacuum environment during the measurement, this technique cannot be duplicated on the solid-liquid interface, to detect the Wenzel state, in which a water droplet completely wets the solid surface, and the Cassie state, in which there is trapped air in the pits to reduce the solid-liquid contact area. Therefore, magnetic alternating current mode atomic force microscope (AFM) is introduced to observe the interface between liquid and solid. P. Chen et al. collected the images of lotus leaf surfaces in the water and in air, by using a small force to drive the cantilever of the AFM probe in water.[4] As the lotus leaf is superhydrophobic, the AFM probe can be immerged in the spherical water droplet to scan the interface between the lotus leaf and water. However, the resolution of this method remains in a microscale range. Therefore, the identification of the interfacial contacts of nanoscale surfaces in solid-liquid interface remains an open challenge.

The second challenge is the instability of nanocomposites with the complicated synthesis methods. Compared to bulk materials, nanomaterials can be oxidized more easily, due to a larger fraction of surface atoms than that of bulk materials. For example, metallic nanoparticles are flammable in ambient conditions. To enhance the stability, a stable thin layer (such as silica) is coated on the metallic nanoparticles to create a core-shell structure. However, this strategy cannot be applied to protect functional nanocomposite surfaces, e.g. superhydrophobic nanocomposite surfaces. Therefore, the intrinsically stable carbon nanotubes are introduced to achieve chemically inert superhydrophobic nanocomposites.

Using high-cost enhanced chemical vapor deposition, Lau et al. fabricated the surface of carbon nanotube nanocomposite, which exhibited remarkable superhydrophobicity.[5] However, the enhanced chemical vapor deposition cannot be used as an industrial process for its high cost. Therefore, various carbon nanotube - conductive polymer nanocomposites were prepared by solvent casting or spray-coating.[6-8] Nevertheless, these conductive polymers degrade under ambient conditions. Therefore, it still remains a challenge to obtain a superhydrophobic surface, which is stable under various stressed conditions, through a widely applicable industrial process.

The final challenge is the under-researched mechanism of the correlation between the interfacial characteristics and the performance of small molecule organic solar cells. Stable small-molecule organic solar cells require the costly vacuum evaporation for fabrication.[9-11] Therefore, solution process, has been introduced to replace the vacuum evaporation. However, solution processed small molecule organic solar cells are less efficient, because of the uncontrolled structural morphology of donor/acceptor interface, which leads to a low fill factor ranging from 24% to 39%.[12-14] Defined as the ratio of the actual maximum obtainable power to the product of short circuit current and open circuit voltage, fill factor is directly determined by series resistance (R_s) and parallel resistance (R_p). To obtain a high fill factor, R_s should be the lower the better, and R_p the higher the better. However, in solution processed small molecule organic solar cells, R_s can be as high as $500\Omega\cdot cm^2$ with a low R_p of about $600\Omega\cdot cm^2$.[12-14] Therefore, in order to improve the fill factor and the power conversion efficiency, it is important to understand the factors that determine the variation of R_s and R_p, and in particular, the relationship between R_s and R_p.

In the equivalent circuit, R_s and R_p are originally introduced as two independent elements. However, from the data in literature, it is found that R_s and R_p are inversely correlated.[14-19] Therefore, it remains a challenging question of, why R_s and R_p are inversely correlated and what is the underlying mechanism behind it.

1.4 Our Answers to the Challenges

Targeting the challenges mentioned above, the main theme of this thesis, therefore, is to investigate the solid-liquid contacts of nanostructured surfaces by direct observation, and to further develop a stable nanocomposite thin film for conducting the observation, and to eventually investigate the effect of interfacial contacts on the performance of organic solar cells.

In order to indentify the solid-liquid contacts of nanostructured surfaces, a direct method of tracing the two different wetting states, the Wenzel and Cassie states, was developed by using Ag nanoparticles as tracing agents. This method provided an answer to a long standing question of, whether there is a transition from Wenzel to Cassie states in the sliding angle drop on nanostructured surfaces. To accomplish the observation, a superhydrophobic nanocomposite thin film with excellent chemical stability was prepared by the spray coating method. To further understand the origin of superhydrophobicity, both the formation of the nano/microstructures and their effects were investigated. Details will be discussed in section 3.1 and 3.2.

Furthermore, with the knowledge of identifying the wetting states and the fabrication process of nanocomposites, a small-molecule nanoparticle organic solar cell with a much improved fill factor was developed by the spin coating method. Series resistance and parallel resistance were discovered to be inversely correlated, due to the variation of the morphology and the change of charge carrier concentrations near the donor and acceptor interface. The inverse correlation between series resistance and parallel resistance contributes to the improvement of the power conversion efficiency of organic solar cells. Details will be discussed in section 3.3 and 3.4.

1.5 Thesis Outline

The current thesis includes four chapters. Chapter 1, *Introduction*, is the current chapter. The outline of remaining chapters is as follows:

Chapter 2, *Background Literature*, provides a general literature review of the nanomaterials and their applications. First of all, the history and applications of nanomaterials are briefly reviewed. Then, the carbon nanotubes and their superhydrophobic nanocomposites are described, followed by an introduction of the synthesis methods of superhydrophobic nanocomposites. After introducing the fundamental knowledge of solid-liquid and solid-solid interfaces, one of the applications of nanomaterials — solar cells, is described.

Chapter 3, which contains two papers and one manuscript, aims to investigate the interfacial contact of nanostructured surfaces involving nanopits of 100nm or less by direct observation, and to develop a stable nanocomposite with hierarchical structure by a low-cost spray coating method, which is needed by the direct observation of the interfacial contact, and to eventually investigate the effect of interfacial contact on the power conversion efficiency of organic solar cells.

Chapter 4, *Summary and Conclusions*, summarizes the key results and presents the most important conclusions of this work.

References

(1) S. R. Emory, and S. Nie, *Science*, **275**, 1102 (1997).

(2) http://www.physorg.com/

(3) A. V. Desai, and M. A. Haque, *Thin-walled Structures* **43**, 1787 (2005).

(4) P. Chen, L. Chen, D. Han, J. Zhai, Y. Zheng, and L. Jiang, *Small* **5**(8), 908 (2009).

(5) K. K. S. Lau, J. Bico, K. B. K. Teo, M. Chhowalla, G. A. J. Amaratunga, and W. I. Milne, *Nano Lett.* **3**, 1701 (2003).

(6) S. Srinivasan, V. K. Praveen, R. Philip, and A. Ajayaghosh, *Angew. Chem. Int. Ed.* **47**, 5750 (2008).

(7) J. Zou, H. Chen, A. Chunder, Y. Yu, Q. Huo, and L. Zhai, *Adv. Mater.* **20**, 3337 (2008).

(8) J. T. Han, S. Y. Kim, J. S. Woo, and G. Lee, *Adv. Mater.* **20**, 3724 (2008).

(9) D. Gebeyehu, M. Pfeiffer, B. Maennig, J. Drechsel, A. Werner, and K. Leo, *Thin Solid Films* **451-452**, 29 (2004).

(10) N. Wang, J. Yu, Y. Zang, J Huang, and Y. Jiang, *Sol. Energy Mater. & Sol. Cells* **94**, 263 (2010).

(11) F. Yang, M. Shtein, and S. R. Forrest, *Nat. Mater.* **4**, 37 (2005).

(12) A. Varotto, C. Nam, I. Radivojevic, J. P. C. Tome, J. A. S. Cavaleiro, C. T. Black, and C. M.Drain, *J. Am. Chem. Soc.* **132**, 2552 (2010).

(13) A. Sanchez-Diaz, R. Pacios, U. Munecas, T. Torres, and E. Palomares, *Org. Electronics* **12**, 329 (2011).

(14) S. Schumann, R. A. Hatton, and T. S. Jones, *J. Phys. Chem. C* 115, 4916 (2011).

(15) J. Xue, B. P. Rand, S. Uchida, and S. R. Forrest, *Adv. Mater.* **17**, 66

(2005).

(16) S. Yoo, B. Domercq, B. Kippelen, *Appl. Phys. Lett.* **85**, 5427 (2004).

(17) M. T. Lloyd, A. C. Tayi, A. M. Bowen, T. G. Kasen, D. J. Herman, D. A. Mourey, J. E. Anthony, and G. G. Malliaras, *Org. Electron.* **7**, 243 (2006).

(18) T. L. Chen, J. J. Chen, L. Catane, and B. Ma *Org. Electron.* **12**, 1126 (2011).

(19) M. Rusu, S. Wiesner, I. Lauemann, Ch. Fischer, K. Fostiropoulos, J. Audinot, Y. Fleming, M. Lux-Steiner, *Appl. Phys. Lett.* **97**, 073504 (2010).

Chapter 2 Background Literature

2.1 History and the Applications of Nanomaterials

2.1.1 Historical Development

Although worldwide interest in nanomaterials is recent, the study on the engineering of many materials such as colloidal dispersions and catalysts has been in the nanometer regime for centuries. For example, the Chinese are known to have used Au nanoparticles as an inorganic dye to introduce red color into their ceramic porcelains for thousands of years. There is also a long history of using colloidal gold nanoparticles in medical applications. Colloidal gold nanoparticles can be used to treat arthritis and to diagnose a number of diseases by observing the interaction of colloidal gold with spinal fluids obtained from patients. The first scientific report on the preparation and properties of colloidal gold was published by Michael Faraday in the middle of 19th century. The colloidal gold nanoparticles prepared by this method stayed stable for almost a century before being destroyed during World War II.

By the early 1940's, silica nanoparticles, which are used as substitutes for carbon black, were synthesized in USA and Germany by precipitation method. Amorphous silica nanoparticles have been applied in many every-day products, ranging from non-diary coffee creamer to sensors, drug carriers and optical fibers.[1] In the 1960s and 1970s metallic nanoparticles for magnetic recording tapes were developed.[2]

Although the applications of nanomaterials lasted over centuries, the concept of nanomaterials was only raised over 40 years ago. Physicist Richard

Feynman delivered a speech in 1959 entitled "There's Plenty of Room at the Bottom", which provided inspiration for the field of nanomaterials. Feynman commented that there were no fundamental physical reasons why materials could not be obtained by manipulating individual atoms, and he suggested that scaling issues would arise from the variation of the magnitude of various physical phenomena.

However, Feynman’s report was neglected in the first twenty years after it was published, due to the absence of instrument innovations. In 1981, the scanning tunneling microscope (STM) (as shown in Figure 2.1), an instrument that allowed scientists to view the world from an atomic level, was developed by Gerd Binnig and Heinrich Rohrer at IBM Zurich Research Laboratory, for which they were awarded the Nobel Prize in Physics in 1986.[3]

The evolvements of STM together with the invention of related instruments have enabled researchers to investigate a wider range of atomic-scale structures and properties with a greater depth. With the help of these novel instruments, even the manipulation of individual atoms and molecules is made possible. For example, IBM scientists had successfully manipulated individual xenon atoms on a nickel surface to spell out the company logo, which can be seen as a show of this great novel technology.

Figure 2.1: The first scanning tunneling microscope invented by Gerd Binnig and Heinrich Rohrer.

However, STM can only be used to observe the conductors and semiconductors. To extend the application, in 1986, Binnig, Calvin Quate and Christoph Gerber invented the first atomic force microscope (AFM) (as shown in Figure 2.2)[4], which provided a three-dimensional surface profile of the conductors, semiconductors, and insulators.

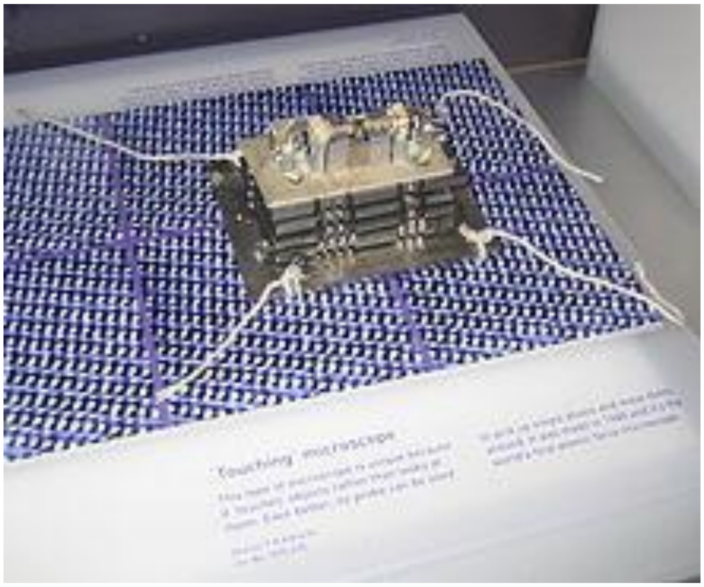

Figure 2.2: The first atomic force microscope.

The innovations of the experimental instruments have greatly accelerated the development of nanomaterials. In the mid-1980s, a new class of material - hollow carbon spheres was discovered (as shown in 2.3(a)), which were named buckyballs or fullerenes, in honor of the architect Buckminster Fuller who designed a geodesic dome with the similar geometry to that of the molecular structure of fullerenes.[5] Fullerenes, which is composed of 60 carbon atoms chemically bonded together in a ball-shaped molecule, has great potential applications in nanotechnology. Therefore, Kroto, Curl, and Smalley, the people who first discovered fullerenes, were awarded the 1996 Nobel Prize in Chemistry.

The discovery of fullerenes has inspired research that led to the synthesis of carbon nanofibers, with diameters under 100 nm. In 1991, S. Iijima of NEC in Japan discovered single walled carbon nanotubes, by adding transition-metal catalysts into carbon in an arc discharge, as shown in 2.3(b).[6] Due to the excellent physical properties, carbon nanotubes and their nanocomposite have attracted more and more research attention in recent years, which will be discussed in section 2.2.1.

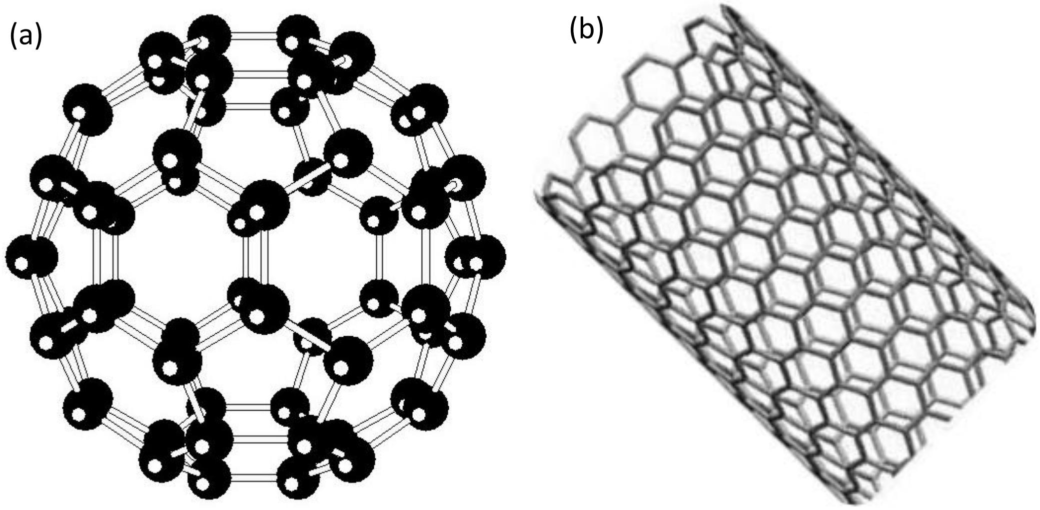

Figure 2.3: (a) The structure of fullerenes; (b) The structure of carbon nanotubes.

In addition to these carbon-based materials, nanoparticles, nanowires, nanorods and nanosized thin films with the chemical composition of metals, inorganic semiconductors, polymers and their nanocomposites have been the focus of the considerable research, due to their remarkable electrical, thermal and mechanical properties. These nanomaterials are valuable for nanotechnology, electronics, optics and other fields of materials science and engineering.

2.1.2 The Applications of Nanomaterials

There is an extremely broad range of potential applications of nanomaterials, from electronic devices (including miniature integrated circuits, organic solar cells), to packaging films, superhydrophobic thin films, and parts of automobiles. While various possible applications and devices have been proposed and studied in the literature, here we only focus on the applications of nanomaterials in the electronic industry.

The application of inorganic solar cells is still limited, due to the high production costs and high energy consumption caused by the manufacturing processes involving high vacuum and numerous lithographic steps. Luckily, the development of nanomaterials provides an opportunity to fabricate low-cost organic solar cells with flexible substrate to replace costly silicon solar cells, as shown in Figure 2.4. Since the diffusion length of the exciton, defined as the average distance that excitons can travel from the point at which they are formed to the point at which they are recombined, is less than 10nm, the development of nano technology enables the creation of nanosized donor and acceptor which is comparable to the exciton diffusion length, and further allows the exciton of the organic solar cells to diffuse to the interface of donor and acceptor materials.

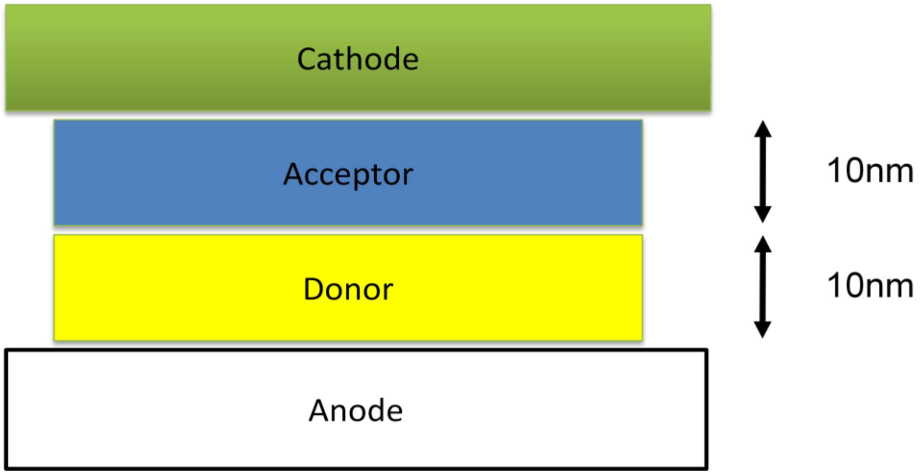

Figure 2.4: Organic solar cells with a nanosized thickness of donor and acceptor.

The microelectronics industry requires minimizing the scale of the devices, whereby the circuits, such as transistors, resistors, and capacitors, are reduced in size. During the reduction in their sizes, the microprocessors, which contain these components, can run much faster, thereby obtain better performance. However, several technological difficulties impedes to these advancements, including gate current leakage as the transistors shrink; poor cooling systems to dissipate heat generated by these microprocessors when run at faster speeds; poor reliability, etc. Nanomaterials help the industry to overcome these barriers by providing the manufacturers with ultra-highly purified nanocrystallines, nanocomposites with better thermal conductivity, and long-lived stable interconnections between the microprocessors.

To minimize the current leakage, hafnium dioxide and titanium dioxide nanosized thin film, which have good insulating properties and could create high capacitance between the gate and the channel, are used to replace the transistor’s silicon dioxide gate dielectric, reducing the gate current leakage by 100-fold.[7] Furthermore, Nanocomposites containing carbon nanotube forests can be applied in the cooling system to conduct heat, due to their excellent thermal conductivity, as shown in Figure 2.5.[8]

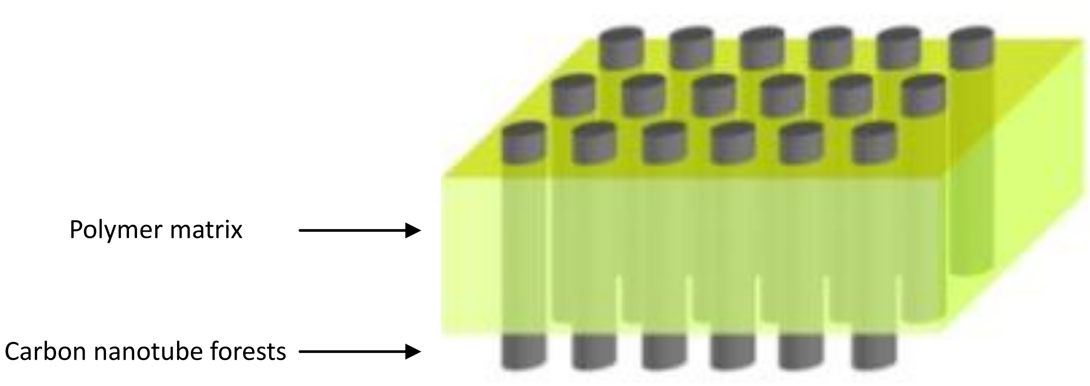

Figure 2.5: The SEM image of the carbon nanotubes-polymer composites with high thermal conductivity.

2.2 Solid-liquid and Solid-solid Interface

The performance of the devices involving nanomaterials are greatly affected by their interfacial characteristics. Therefore, the two major interfacial contacts: solid-liquid and solid-solid contacts will be introduced in this section.

2.2.1 Two Wetting States

The wettability of the solid surface by a liquid droplet can be measured by the contact angle which could be expressed by Young's equation on the smooth surface as shown in Figure 2.6.[9,10]

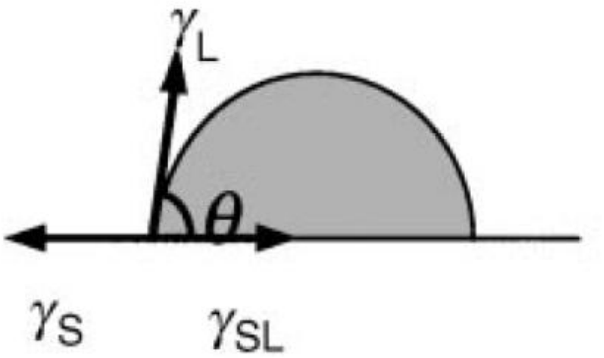

Figure 2.6: The contact angle of a liquid droplet on the smooth surface.

In Young's equation, γ_S indicates the surface energy between the solid and air; γ_{SL} represents the surface energy between the solid and the liquid, and the γ_L indicates the surface energy between the liquid and air. Nanostructured surfaces with water contact angle larger than 90° are called hydrophobic materials. In contrast, surfaces are referred to as hydrophilic surfaces if the water contact angle is less than 90°.[11-13] If the water contact angle of a surface is greater than 150°, the surface is known as a superhydrophobic surface.[11-13]

Two models have been proposed to explain the variation of contact angles: while the first model—the Wenzel model (as shown in Equation ①) relates the contact angle to the surface roughness, the other model—the Cassie model (as shown in Equation ②) is based on the contact area fraction versus solid-liquid interaction.[14,15] These two models describe two distinctive wetting behaviors of a liquid droplet. In the case of the Wenzel model, a water droplet completely wets the surface in spite of the existence of pits and asperities, resulting in an intimate liquid-solid contact (see Figure 2.7(a)). Conversely, in the Cassie state, air is assured to be trapped in the pits between asperities, thus the contact area is reduced to cover only the top parts of the protruding elements, and making for a much smaller than the apparent water-solid interface (see Figure 2.7(b)).

$$\cos\theta_W = \frac{r\gamma_S - r\gamma_{SL}}{\gamma_L} = r\frac{\gamma_S - \gamma_{SL}}{\gamma_L} \qquad ①$$

$$\cos\theta_C = \Phi_S \cos\theta + \Phi_S - 1 \qquad ②$$

In Equation ①, the contact angle of the rough surface ($\cos\theta_W$) is determined by the surface energy of the solid-liquid interface (γ_{SL}), solid-air interface (γ_S), liquid-air interface (γ_L) and the ratio of real surface area to nominal surface area in horizontal direction (r, $r \geqslant 1$). On the contrary, as shown in Equation ②, the contact angle ($\cos\theta_C$) is related to the fraction of contact area of liquid-solid interface (Φ_S) and the intrinsic contact angle of the smooth surface.

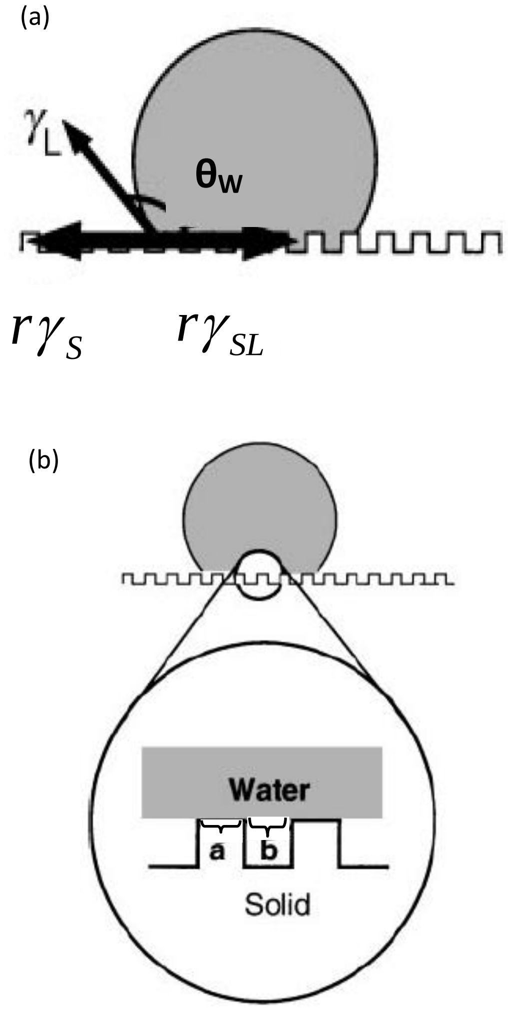

Figure 2.7: (a) The Wenzel model; (b) The Cassie model, “a” represents the contact area of liquid-solid interface; conversely, “b” represents the contact area when air is trapped.

2.2.2 Ohmic Contact

Having a lineal current – voltage characteristic, an ohmic contact is used in the connection of electronic components in integral circuits, providing minimal resistance and no tendency to rectify signals.[16] Taking the contact between metals and n-type semiconductors as an example, the energy band diagram of an ohmic contact is described as follows. In the energy band diagram of n-type semiconductor-metal contact as shown in Figure 2.8, E_{fm} is the Fermi level of metal; E_C E_F, and E_V represent the conduction band, Fermi level of n-type semiconductor, and valence band, respectively. Before contact, metals and n-type semiconductors, in which electrons are major charge carriers, have different work functions, described as φ_M and φ_S ($\varphi_M > \varphi_S$) respectively.

When the two materials are placed in contact (Figure 2.8), the electrons are transferred from metal to semiconductor to align the Fermi level at equilibrium. This raises the semiconductor electron energy relative to the metal and leads to a small energy barrier, which can be easily overcome by a small voltage. The reason for a small energy barrier is that no depletion region occurs in the semiconductor, since the required electrostatic potential to align the Fermi level is caused by the accumulation of majority carriers in the semiconductor.

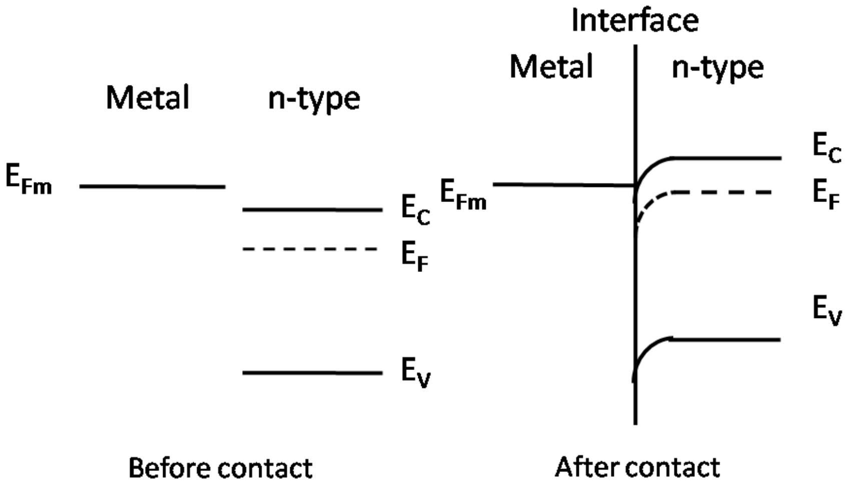

Figure 2.8: The energy band diagram of an ohmic contact caused by contacting an n-type semiconductor with a metal having a smaller work function.

2.2.3 p-n Junction and Schottky Barrier

A p-n junction is created when a p-type and an n-type semiconductor are placed in contact with each other. The p-n junctions are usually used as diodes in integrate circuits, which allows current flow more easily in one direction than the other. Unlike an ohmic contact, in p-n junctions, the current – voltage characteristic is non-linear, due to the existence of an energy barrier at the p-n junction interface.

In the energy band diagram shown in Figure 2.9, after joining the p-type and n-type semiconductors, the electrons of the n-type semiconductor flow to the p-type semiconductor to align the two Fermi levels, leaving fixed positive ions in the n region. Similarly, the fixed negative ions are also left in the p region, when holes of the p-type semiconductor flow to n-type semiconductor. Therefore, at equilibrium, an electric field is generated by these fixed positive/negative ions near the interface of the p-n junction. Then, the energy band diagram after contact can be obtained by combining the electric potential energy of the p-n junction with the energy band before contact. Therefore, the energy barrier is formed, due to the rise of the p-type semiconductor electron energy relative to the n-type.

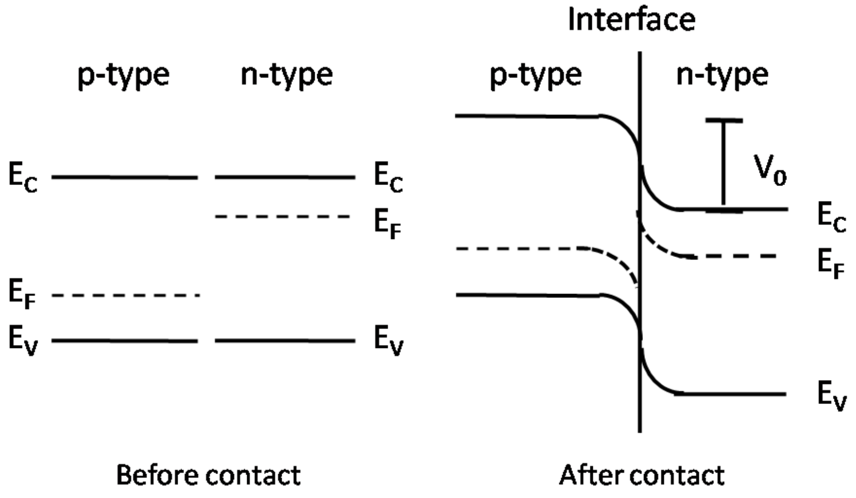

Figure 2.9: The energy band diagram of a p-n junction.

After applying a forward bias voltage (V) to a p-n junction (p side: positive), the energy barrier becomes lower and lower, because the forward bias voltage raises the energy band of p side relative to n side. When $V>V_0$, as shown in Figure 2.9, the current increases sharply with the forward bias.

Very similar to p-n junction devices, Schottky barrier devices, which contain a metal-semiconductor contact, can be used as a rectifying component in circuits. For the contact between the n-type semiconductor and metal as shown in Figure 2.10, when $\varphi_M < \varphi_S$, the Fermi level of semiconductor is initially higher than that of metal before the contact. At equilibrium, to align the two Fermi levels, the electrons flow from n-type semiconductors to metals, leading to an energy barrier near the interface between n-type semiconductors and metals.

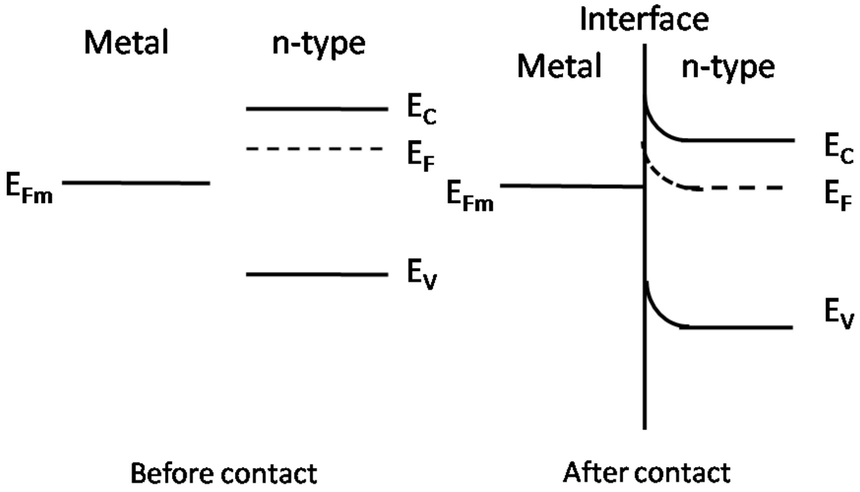

Figure 2.10: The energy band diagram of a Schottky barrier caused by contacting an n-type semiconductor with a metal having a smaller work function.

2.3 Superhydrophobic Nanocomposites

Superhydrophobic nanocomposite surfaces have a water contact angle larger than 150º and sliding angles smaller than 5º. The formation of superhydrophobic surfaces is determined by surface chemistry and surface structure. On the one hand, composites containing –CF_3 groups can provide the lowest surface energy that is required for the formation of superhydrophobic surfaces.[17] On the other hand, rough surface structure could increase the water contact angle by increasing surface roughness to a certain extent.[17,18] Although these two factors both contribute to the increasing water contact angle, none of them could provide superhydrophobic surface separately. Superhydrophobic surfaces, therefore, are obtained by combining materials with low surface energy and high surface roughness.[19]

In nature, many natural species exhibit water contact angles higher than 150°, such as lotus leaves, and water strider's legs, *etc*.[20] These natural superhydrophobic surfaces are all covered by low surface energy materials and have dual scale structures--microscale structure and nanoscale structure. For example, the lotus leaf with a water contact angle of 161± 2.7° has the sliding angle of less than 2°.[21] The SEM picture obtained by Barthlott and Neihuis reveals that the lotus leaf consists of a combination of microscale bumps in the size of 10μm and nanoscale bumps in the size of 100nm. The hydrophobicity of a lotus leaf arises from the hydrophobic wax which has the water contact angle of 110°.[22-24] It is suggested that the combination of the hierarchical structure and wax contributes to the superhydrophobicity of the lotus leaf.[25,26]

In the following sections, carbon nanotubes (CNTs) and their superhydrophobic nanocomposites, as well as the general preparation methods of the superhydrophobic nanocomposites are discussed.

2.3.1 Carbon Nanotubes and Their Superhydrophobic Nanocomposites

Carbon nanotubes (CNTs), including single-walled carbon nanotubes and multi-walled carbon nanotubes, together with their nanocomposites, have attracted intensive attention in the past 30 years due to their excellent electronic, mechanical and hydrophobic properties,[27-29] and have found potential applications in compliant interconnect structures,[30] solar cells,[31,32] stable self-cleaning thin films,[33] light-emitting diodes,[34] and field-effect transistors.[35]

Most single-walled nanotubes have a diameter of about 1 nanometer, and have a tube length which is several million times longer than the diameter. Carbon nanotubes can be conceptualized as a rolled up sheets of graphene as shown in Figure 2.11.[36] The way that a graphene sheet is wrapped is described by a pair of indices (n, m), as shown in Figure 2.12.[37] The integers n and m represent the number of unit vectors along two directions in the honeycomb crystal lattice of graphene (a_1 and a_2 in Figure 2.12). If $m = 0$, the nanotubes are named zigzag nanotubes, and if $n = m$, the nanotubes are named armchair nanotubes. Otherwise, they are called chiral nanotubes. Using the same method, multi-walled carbon nanotubes are composed of multiple rolled layers of graphene.

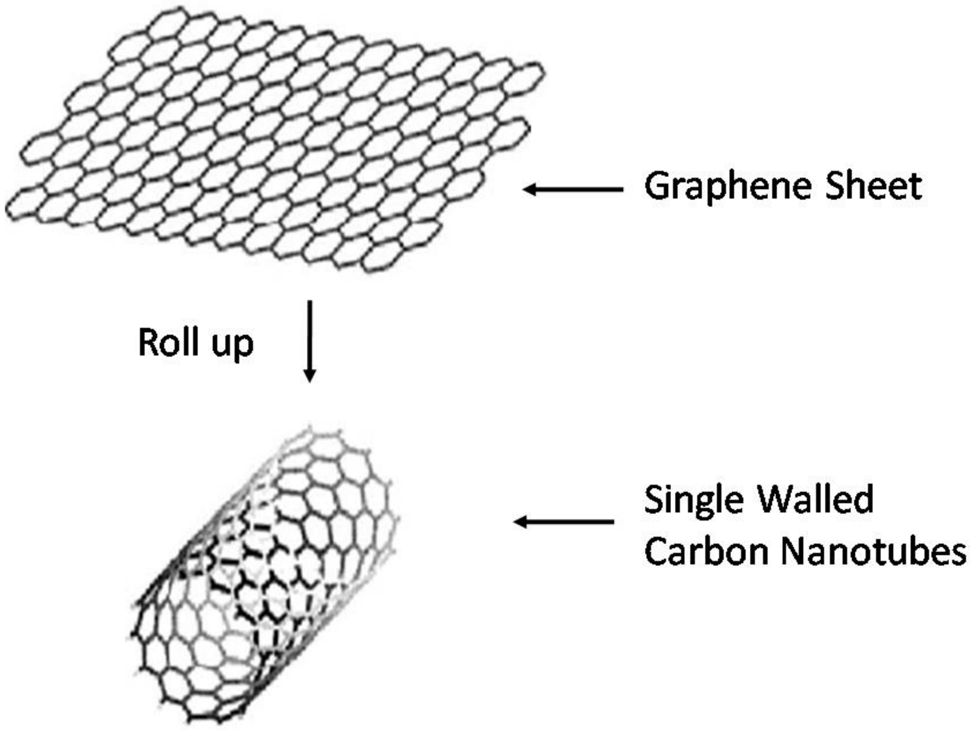

Figure 2.11: The formation of a single walled carbon nanotube.

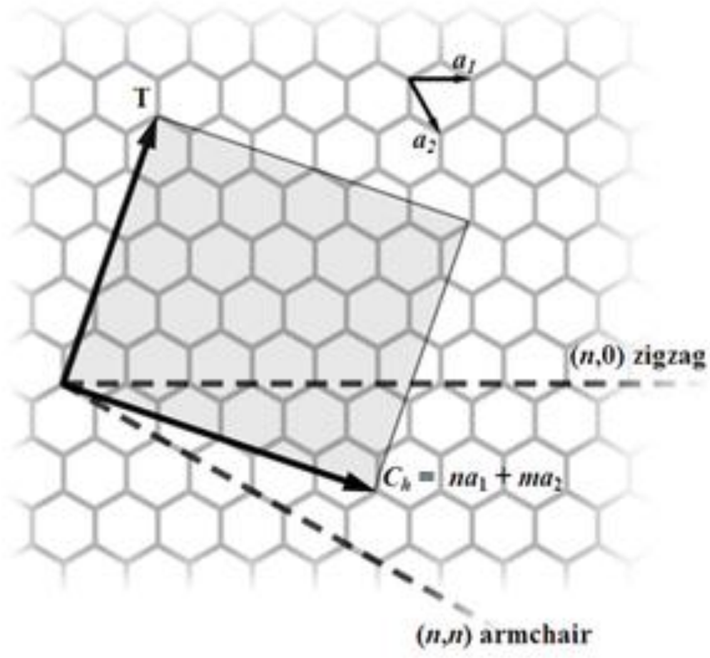

Figure 2.12: The scheme of “rolling up” the graphene sheet to make (n, m) carbon nanotubes, T represents the tube axis, and a_1 and a_2 are the unit vectors of graphene.

The properties of the carbon nanotubes are largely determined by their symmetric structures, and these properties can be best exploited by incorporating the nanotubes into some form of matrix (usually, polymers). Right now, the superhydrophobic nanocomposites containing carbon nanotubes are discussed here. Carbon nanotubes are used in the superhydrophobic nanocomposites, due to their excellent stability. Table 2.1 shows the parameters of the superhydrophobic nanocomposites containing carbon nanotubes in literature.

Table 2.1: The superhydrophobic nanocomposites containing carbon nanotubes.

Choices of Materials	Contact angle	Sliding angle	Preparation method	Ref.
CNT forests polytetrafluoroethylene	169 ^{o}	8 ^{o}	Chemical vapor deposition	38
olig(p-phenylenevinylene)s-graft CNTs	165 ^{o}	2 ^{o}	Drop coating	39
poly(3-hexylthiophene)-block-polystyrene-graft CNTs	159.9 ^{o}	<5 ^{o}	Drop coating	40
Silica, tetraethoxysilane, CNTs	153 ^{o}	>10 ^{o}	Spray coating	41

2.3.2 Top-down Synthesis

Extensive research has been applied to the fabrication of superhydrophobic thin films. The processes that are developed to develop a superhydrophobic surface can be divided into two categories: top-down processes and bottom-up processes. Top-down processes, such as template methods, and plasma treatments, construct materials by nano-molding or cutting bulk materials with nano-imprinter or chemical agents. On the contrary, bottom-up processes such as chemical depositions, layer-by-layer depositions, and sol-gel methods, fabricate nanomaterials by assembling molecules or atoms into blocks. The main purpose of these methods is to create desired surface structure by a facile method.

As a general term used in microelectronics, top-down methods refer to approaches used to prepare materials and devices by machining the bulk materials with cutting tools and laser methods, or by casting in a mold. For the preparation of superhydrophobic surface through top-down methods, several approaches can be adopted to create the required surface roughness. In order to replicate the surface morphology, lotus leaves were initially used as molds,[42,43] followed by two synthesized templates: anodic aluminum oxide (AAO) and poly(urethane acrylate) (PUA).[44-46] In the treatment of plasma etching, CF_4, SF_6 plasmas generated from an inductively coupled plasma (ICP) reactor can obtain the desired surface roughness as well.[47-49] Apart from plasmas, acids or bases can also be applied to etch the substrate in the fabrication of a superhydrophobic surface.[50,51]

M. Sun et al.[42] created a superhydrophobic nanocomposite using a lotus leaf as a template, by the method of nanoscale casting. As shown in Figure 2.13(a), a negative replica of a lotus leaf was obtained by casting poly-(dimethylsiloxane) (PDMS) onto the lotus leaf surface. Afterwards, the superhydrophobic positive replica was achieved by casting a second layer of PDMS onto the negative replica. According to the SEM image in Figure 2.13(b), the nanosized hills and valleys exhibit the similar morphology to the lotus leaf template.

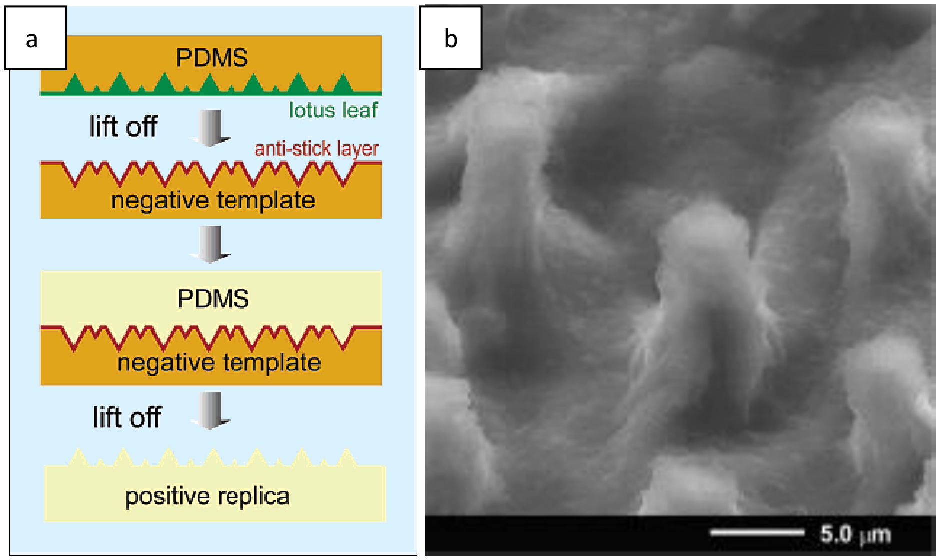

Figure 2.13: (a) The scheme of the preparation of PDMS superhydrophobic surface; (b) The SEM image of the positive PDMS replica.

As the lotus leaf template cannot be industrialized, Lee et al.[44] applied anodic aluminum oxide (AAO) to prepare superhydrophobic thin films. As shown in Figure 2.14, after pressing the polystyrene (PS) film onto the AAO substrate at certain pressure, the polystyrene films was heated to a temperature slightly above its glass transition temperature. Then the morphology of the AAO substrate was successfully negatively replicated on the PS thin films. Finally, the contact angle of the superhydrophobic surface achieved was as large as 160 º.

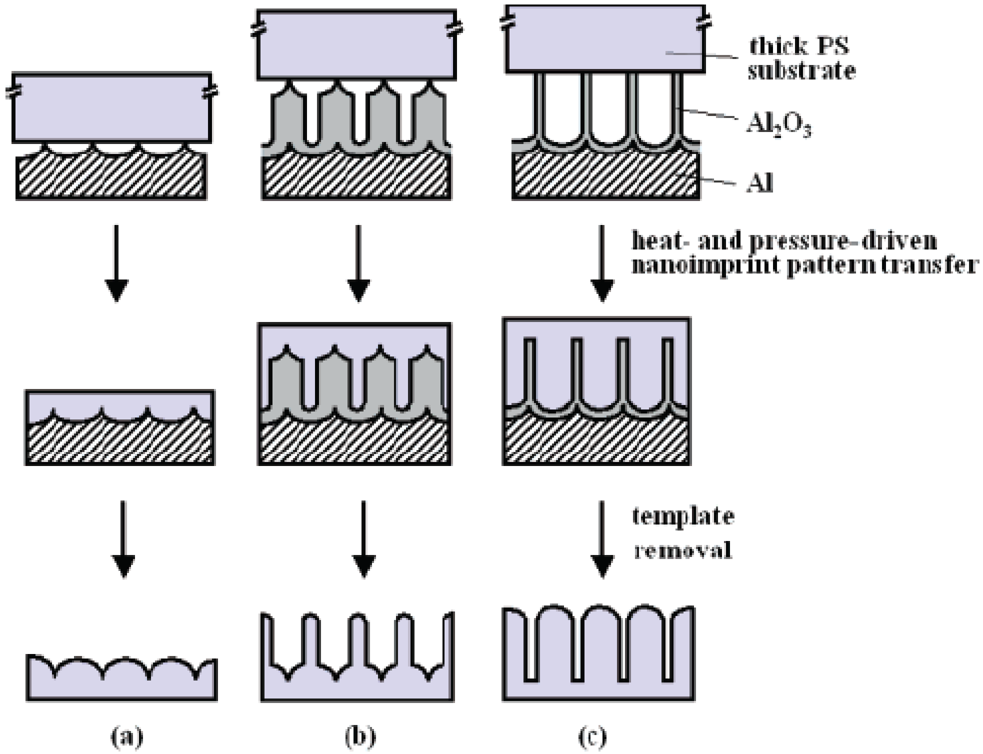

Figure 2.14: Schematic outline of the fabrication for polystyrene superhydrophobic surface.

Tserepi et al.[47] treated PDMS in SF_6 plasmas that were generated in an inductively coupled plasma (ICP) reactor, in order to form the PDMS forest with the height of 1.45 microns. During etching the PDMS surfaces, the C_4F_8 was deposited onto the surface. It has been verified that the dimensions of the pillars were proportional to the etching time of SF_6 plasmas.

In another process, Y. Kwon et al.[49] combined two etching techniques, namely the standard deep silicon etching technique and the moderate gas phase isotropic etching to fabricate a superhydrophobic thin film on silicon wafers. The contact angle of the superhydrophobic surface is greater than 170 °.

2.3.3 Bottom-up Assembly

As opposed to top-down methods, bottom-up methods involve integrating a large amount of building blocks (e.g. nanomaterials or molecules) together into nanocomposites. Self-assembly is the basis of bottom-up methods, where components spontaneously assemble in a solution or gas phase until a stable structure with minimum surface energy is reached. Bottom-up methods have already been applied to the preparation of a superhydrophobic surface through methods such as chemical deposition,[52,53] layer by layer methods,[54] and sol-gel methods[55,56]. Examples of bottom-up methods are presented in the following paragraphs.

K. Tadanaga et al.[52] prepared an Al_2O_3 superhydrophobic thin film by hydrolysis methods. The aluminum tri-sec-butoxide and isopropyl alcohol were mixed at room temperature with constant stirring, followed by the addition of ethyl acetoacetate as a chelating agent. Then, deionized water was added into the mixed solution for hydrolysis, giving a flowerlike Al_2O_3 nanostructured surface. Finally, Heptadecafluorodecyl- trimethoxysilane was coated on the flowerlike structure as a water-repellent agent. The contact angle of the obtained film is 165 °. W. Wu, et al,[53] fabricated $[CH_3(CH_2)_{10}COO]_2Cu$ nanorod thin films by spraying $[CH_3(CH_2)_{10}COO]_2Cu$ emulsion onto glass, aluminum, or other substrates. After the emulsion vaporized on the substrate, nanorods with the diameter of 250nm-300nm and the length of several micrometers spontaneously assembled on the substrates. This fluorine-free superhydrophobic thin film can be repaired by simply re-spraying if it is damaged.

K. Liao et al.[54] achieved an ultrathin superhydrophobic thin film containing grafted carbon nanotubes (CNT-NH-PEI) through layer-by-layer methods. The CNT-NH-PEI were prepared by grafting amine (NH) functional groups of polyethyleneimine (PEI) to carbon nanotubes in N,N-dimethylformamide (DMF). Then, the polyacrylic acid treated polyethylene thin film was placed into the suspension of CNT-NH-PEI (cationic solution) and polyacrylic acid (anionic solution) in turns, in order to fabricate superhydrophobic thin films by ionic attractions. These superhydrophobic thin films obtained show a contact angle of 164 °together with a sliding angle of 5 °. Shang et al.[55] prepared transparent superhydrophobic thin films by sol-gel method. The superhydrophobic thin film achieved demonstrated an optical transparency higher than 90%.

2.4 Solar Cells

2.4.1 Silicon Solar Cells and Organic Solar Cells

Solar cells are devices that convert visible light to electricity directly. Right now, silicon solar cells, which are used in small power stations, handheld calculators and wrist watches, are dominating the solar cell market with energy efficiency of up to 20%.[57] A complete silicon solar cell is composed of two electrodes, p/n silicon junction and an optional anti-reflection coating, used to trap photons within the silicon solar cells. Please see Figure 2.15 for the visual structure of silicon solar cells.

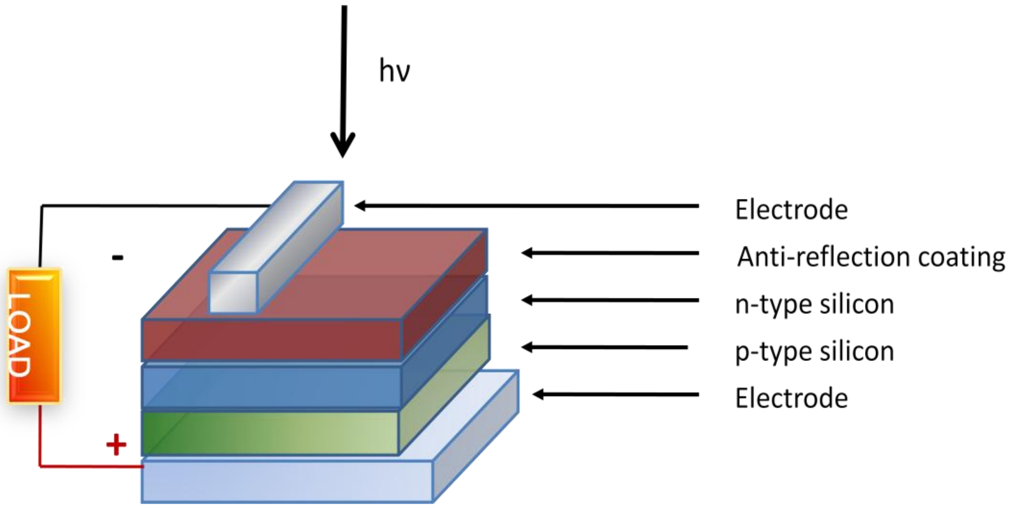

Figure 2.15: The structure of silicon solar cells.

Although silicon solar cells dominate the solar cell market, the manufacturing processes of this type of solar cell often involve costly, high vacuum, and numerous lithographic steps, leading to a high production cost and high energy consumption.[58,59] Compared to the silicon solar cells, organic solar cells can be mechanically flexible, cost less, and can be fabricated under normal ambient conditions through low-cost processing methods. It is for these reasons that organic solar cells are very promising devices that may replace silicon solar cells.[60]

There are two kinds of organic solar cells: small molecule organic solar cells and polymer organic solar cells. The typical donor/acceptor pairs are copper phthalocyanine (CuPc)/ C_{60} for small molecule organic solar cells, and poly-3(hexylthiophene) (P3HT)/ phenyl-C61-butyric-acid-methyl ester (PCBM) for polymer organic solar cells, as described in Table 2.2. As to the fabrication process for these two types of organic solar cells, vacuum evaporation is commonly used to fabricate small molecule organic solar cells, while the solution process (e.g. spin coating) is applied to construct polymer solar cells.[61-63] During the fabrication, both the bilayer and bulk heterojunction structures can be obtained in these two types of organic solar cells, which will be further discussed in section 2.4.3.

Table 2.2: The comparison between small molecule organic solar cells and polymer organic solar cells.

	Small molecule organic solar cells	Polymer organic solar cells
Donor	Small molecule (eg: CuPc)	Polymer (eg: P3HT)
Acceptor	C_{60}	PCBM
Process types	Vacuum evaporation	Solution process:
Structure types	Bilayer structure Bulk heterojunction structure	

2.4.2 Working Principles

The procedure of converting light into electricity includes four steps which are described in the energy band diagram, as shown in Figure 2.16.

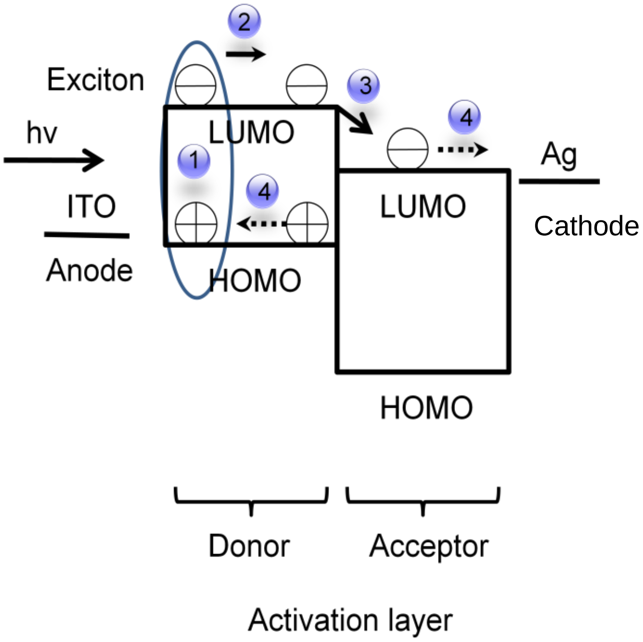

Figure 2.16: Working principles of organic solar cells.

(1) After the absorption of a photon, an exciton is generated.

(2) Excitons diffuse to the donor/acceptor interface.

(3) Excitons are separated by the electric field into electrons and holes.

(4) The electrons are transported to the cathode and the holes to the anode, respectively.

The current density of the organic solar cells is determined by the number of charge carriers that reach the electrodes per unit time. This number is related to the fraction of photons absorbed, the fraction of generated excitons that are separated, and the fraction of separated charge carriers collected at the electrodes. The faction of absorbed photons is influenced by the thickness of the absorption layer, the absorption coefficient and absorption spectrum of the donor and acceptor materials. The fraction of generated excitons that are separated is largely determined by the diffusion length of excitons and the structure of the organic solar cell, which will be described in section 2.4.4.

In order for charge carriers to reach the electrodes, two kinds of driving force contribute to the transport of charge carriers. On the one hand, the internal electric fields induce drift current of the charge carriers. On the other hand, the concentration gradients lead to diffusion currents. In organic solar cells, the drift current is dominant, due to the fact that the thickness of activation layer is less than 100nm.[64,65]

2.4.3 Current Density-Voltage Curve and Equivalent Circuit Analysis

The energy efficiency and other photovoltaic parameters of organic solar cells can be obtained from the current density – voltage characteristics, as shown in Figure 2.17.

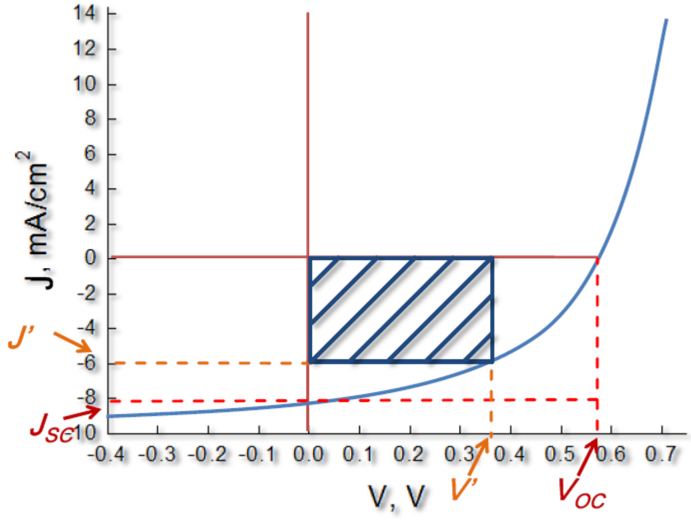

Figure 2.17: The current density (J) – voltage (V) characteristics of organic solar cells.

Under illumination, the open circuit voltage (V_{oc}), which represents the largest output voltage of organic solar cells, is achieved when there is no photo-generated current. The maximum photocurrent, named as short circuit current (J_{sc}), is obtained under the short-circuit condition (V=0). Between V_{oc} and J_{sc}, in the forth quadrant, the organic solar cells generate power under different load resistances. The maximum power can be obtained at the point when the product of the V_{oc} and J_{sc} is largest. There is another important parameter, the fill factor (FF), which is defined as the maximum obtainable power over the product of the V_{oc} and J_{sc}. Therefore, efficiency of a organic solar cell is described as follows:

$$\eta\% = \frac{\mathrm{P_{output}}}{\mathrm{P_{input}}} = \frac{\mathrm{J}_{SC} V_{OC} FF}{\mathrm{P_{input}}}$$

Therefore, the energy efficiency of organic solar cells is determined by the V_{oc}, J_{sc} and fill factor. A closer look at the energy efficiency indicates that V_{oc} is determined by the energy band gap of donor and acceptor materials and the work function of the electrodes.[66] J_{sc} is largely determined by the interfacial area of donor and acceptor materials.[67-69] The fill factor, which describes the squareness of the current density – voltage curve, is determined by the series resistance (R_S) and parallel resistance (R_p) of organic solar cells, which is described through the equivalent circuit as shown in Figure 2.18.[70]

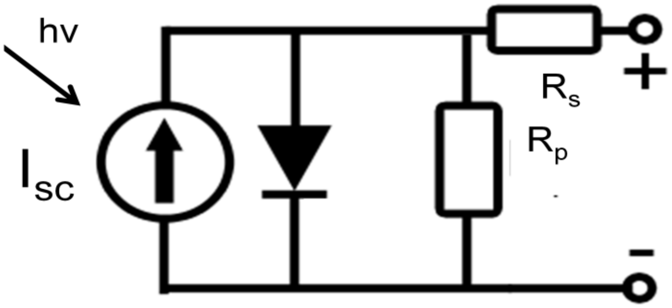

Figure 2.18: Equivalent circuit of organic solar cells.

According to the equivalent circuit, to achieve a high fill factor, the R_s, which is composed of the bulk resistance and the interfacial resistance, should ideally be as low as possible. In contrast, the R_p, which represents the recombination of electrons and holes should ideally be as high as possible.

To sum up, the current density-voltage curve and the equivalent circuit are helpful for us to understand the various photovoltaic parameters and the correlation between these parameters and energy efficiency.

2.4.4 The Structures of Organic Solar Cells

There are three kinds of structures in organic solar cells-- the single layer structure, the bilayer structure, and the bulk heterojunction structure.

The first type of organic solar cell was based on the single layer structure, which is composed of a p-type organic semiconductor sandwiched by two electrodes. Usually, ITO glass served as the transparent anode to collect holes, while a layer of metal such as Al and Ca was used as the cathode to collect electrons.[71] The structure of single layer organic solar cells is depicted in Fig. 2.19, where the structure is ITO/p-type organic semiconductor/Al.

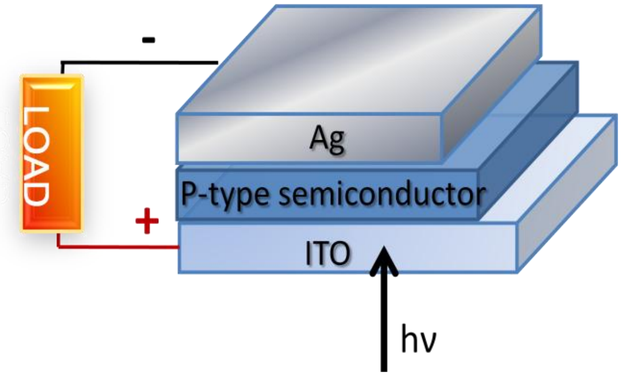

Figure 2.19: The structure of single layer organic solar cells.

At equilibrium, a Schottky barrier is formed between the interface of the p-type organic semiconductor and Al, which provides the electric field to separate the excitons into electrons and holes. However, the efficiency of the single layer solar cells is usually less than 0.1%, because the thickness of the organic film is less than 10nm, leading to the poor absorption of light. The reason for the thin organic film is that the diffusion length of the exciton, defined as the average distance the exciton moves from generation to recombination, is less than 10nm for most organic semiconductors. Furthermore, the depletion region of the Schottky barrier is very thin, which leads to more recombination of charge carriers before and after charge separation.

To increase the absorption of light and the fraction of the separated excitons, the bilayer structure was proposed, as shown in Figure 2.20. In the bilayer structure, electron donor and electron acceptor layers, which are called activation layers, are stacked to form a planar interface. The thickness of the bilayer organic solar cells has been pushed to 20-40nm in total.[72] However, the efficiency is still limited, due to the small interfacial area of the donor and acceptor interface.

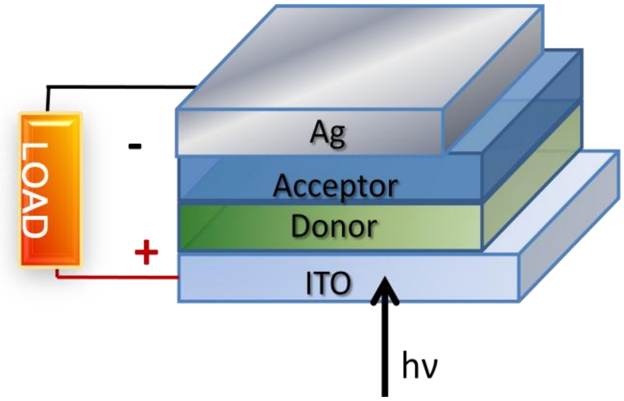

Figure 2.20: The structure of bilayer organic solar cells.

To improve the low efficiency of bilayer structured organic solar cells, the structured heterojunction was introduced to enlarge the interfacial area. This was achieved by coating the donor and acceptor materials in such a way as to have the two materials form an nanoscale interpenetrating network.[73-75] Therefore, more excitons can reach the interface before the recombination, leading to a huge improvement of energy efficiency.

In the structured heterojunction, the donor and acceptor materials are intimately mixed. As there is no preferred direction for the internal electric fields of separated charges, only the concentration gradient can act as the driving force for charge transport. In this case, not all the charge carriers move to the electrodes and the electron-hole recombination increases. Therefore, electrodes with different work functions are used here to provide a drift driving force by forming an electric field between the two electrodes.

2.4.5 Constructions of Organic Solar Cells

Vacuum evaporation and solution process are the common techniques used in the preparation of organic solar cells. Vacuum evaporation is a clean method to deposit small molecules. A vacuum chamber equipped with a cryopump is applied to reduce the contamination of water and oxygen during the vacuum evaporation. All of the deposition is performed under a vacuum of $5*10^{-5}$ Torr. During the evaporation, chamber pressure is monitored using a micro-ion sensor and the thickness of the thin films was measured by a quartz crystal oscillator. By alternating the relative position of the quartz crystal oscillator and the sample, a very thin layer (<1nm) can be deposited. However, this method requires costly vacuum during fabrication, which presents a huge capital cost for manufacturing.

Conversely, solution processing (e.g. low-cost spin coating), can be applied in ambient conditions to form a homogenous large-area thin film. After dissolving the donor and acceptor materials in an organic solution, several drops of the mixture are placed on the substrate. The substrate is rotated at a high speed in order to spread the fluid and wet the entire substrate. The thin films with desired thickness can be obtained by controlling the spin speed, rotational acceleration speed, and deceleration speed. Because of the low production cost, the solution processing method has been dominant in the fabrication of polymer based organic solar cells and begins to replace the vacuum evaporation in small-molecule organic solar cells.

References:

(1) I. I. Slowing, B. G. Trewyn, S. Giri and V. S. Y. Lin, *Adv. Func. Mater.* **17**, 1225 (2007).

(2) M. N. Rittner, and T. Abraham, *JOM J. Miner., Metals and Mater. Soc.* **50**, 37 (1998).

(3) www.research.ibm.com/

(4) http://en.wikipedia.org/

(5) P. Ravi, S. Dai, C. Wang, and K. C. Tam, *J. Nanosci. & Nanotech.* **7**, 1176, (2007).

(6) S. Iijima, *Nature* **354**, 56 (1991).

(7) http://www.intel.com/technology

(8) H. Huang, C. Liu, Y. Wu, and S. Fan, *Adv. Mate.* **17**(13), 1652 (2005).

(9) D. Quere, *Annu. Rev. Mater. Res.* **38**, 71 (2008).

(10) L. Gao, and T. J. McCarthy, *Langmuir* **23**, 3762-3765 (2007).

(11) G. Carbone, L. Mangialardi, *Eur. Phys. J. E* **16**, 67 (2005).

(12) P. S. Swain, and R. Lipowsky, *Langmuir* **14**, 6772 (1998).

(13) A. Marmur, *Langmuir* **19**, 8343 (2003).

(14) R. N. Wenzel, *Ind. Eng. Chem.* **28**, 988 (1936).

(15) A. B. D. Cassie, and S. Baxter, *Trans. Faraday. Soc.* **40**, 546 (1944).

(16) D. K. Scheoder, and D. L. Meier, *IEEE Trans. Electron. Dev.* **5**, 637 (1984).

(17) D. Quere, *Physica A* **313***,* 32 (2002).

(18) E. Bormashenko, *Colloids and Surfaces A: Physicochem. Eng. Aspects* **324**, 47 (2008).

(19) M. Nosonovshy, and B. Bhushan, *J. Phys.: Condens. Matter* **20**, 225009 (2008).

(20) D. P. Holmes, M. Ursiny, and A. J. Crosby, *Soft Matter* **4**, 82 (2008).

(21) K. Didemner, and T. J. McCarthy, *Langmuir* **16**, 7777 (2000).

(22) J. Genzer, and K. Efimenko, *Biofouling* **22**, 339 (2006).

(23) H. Liu, J. Zhai, and L. Jiang, *Soft Matter* **2**, 811 (2006).

(24) M. Ma, R. M. Hill, and G. C. Rutledge, *J. Adhesion Sci. & Tech.* **22**, 1799 (2008).

(25) F. Eisenhaber, *Perspec. Drug Dis. & Design* **17**, 27 (1999).

(26) D. Quere, and M. Reyssat, *Phil. Trans. R. Soc.* **366**, 1539 (2008).

(27) N. Sazonova, Y. Yaish, H. Ustunel, D. Roundy, T. A. Arias, and P. L. McEuen, *Nature*, **431**, 284 (2004).

(28) A. Srivastava, O. N. Srivastava, S. Talapatra, R. Vajtai, and P. M. Ajayan, *Nature Mater.* **3**, 610 (2004).

(29) B. J. Hinds, N. Chopra, N. Rantell, R. Andrews, V. Gavalas, and L. G. Bachas, *Science* **303**, 62 (2004).

(30) A. Y. Cao, P. L. Dickrell, W. G. Sawyer, M. N. Ghasemi-Nejhad,and P. M. Ajayan, *Science* **310**, 1307 (2005).

(31) H. Zhou, A. Colli, A. Ahnood, Y. Yang, N. Rupesinghe, T. Butler, I. Haneef, P. Hiralal, A. Nathan, and G. Amaratuna, *Adv. Mater.* **21**, 3919 (2009).

(32) Q. Shu, J. Wei, K. Wang. H. Zhu, Z. Li, Y. Jia, X. Gui, N. Gao, X. Li, C. Ma, and D. Hu, *Nano Lett.* **9**, 4338 (2009).

(33) C. Luo, X. Zuo, L. Wang, S. Song, J. Wang, L. Wang, C. Fan, and Y. Cao, *Nano Lett.* **8**, 4454 (2008).

(34) K. Lee, Z. Wu, Z. Chen, F. Ren, S. J. Pearson, and A. G. Rinzler, *Nano Lett.* **4**, 911 (2004).

(35) Z. Wu, Z. Chen, X. Du, J. M. Logan, J. Sippel, M. Nikolou, K. Kamaras, J. R. Reynolds, D. B. Tanner, A. F. Hebard, and A. G. Rinzler, *Science* **305**, 1273

(2004).

(36) A. V. Desai, and M. A. Haque, *Thin-walled Struct.* **43**, 1787 (2005).

(37) T. Belin, and F. Epron, *Mater. Sci. Eng. B* **119**, 105 (2005).

(38) K. K. S. Lau, J. Bico, K. B. K. Teo, M. Chhowalla, G. A. J. Amaratunga, W. I. Milne, G. H. McKinley, and K. K. Gleason, *Nano Lett.* **3**, 1701 (2003).

(39) S. Srinivasan, V. K. Praveen, R. Philip, and A. Ajayaghosh, *Angew. Chem. Int. Ed.* **47**, 5750 (2008).

(40) J. Zou, H. Chen, A. Chunder, Y. Yu, Q. Huo, and L. Zhai, *Adv. Mater.* **20**, 3337 (2008).

(41) J. T. Han, S. Y. Kim, J. S. Woo, and G. Lee, *Adv. Mater.* **20**, 3724 (2008).

(42) M. Sun, C. Luo, L. Xu, H. Ji, Q. Ouyang, D. Yu, and Y. Chen, *Langmuir* **21**, 8978 (2005).

(43) B. He, N. A. Patankar, and J. Lee, *Langmuir* **21**, 4999 (2005).

(44) W. Lee, M. Jin, W. Yoo, and J. K. Lee, *Langmuir* **20**, 7665 (2004).

(45) J. Ye, Q. Yin, and Y. Zhou, *Thin Solid Films* **517**, 6012 (2009).

(46) K. Y. Suh, and S. Jon, *Langmuir* **21**, 6836 (2005).

(47) A. D. Tserepi, M-E. Vlachopoulou, and E. Gogolides, *Nanotechnology* **17**, 3977 (2006).

(48) Y. Yan, M. B. Chan-Park, and C.Y. Yue, *Langmuir* **21**, 8905 (2005).

(49) Y. Kwon, N. A. Patankar, and J. Choi, Lee, J. *Langmuir* **25**, 6129 (2009).

(50) A. Guo, F. Zhou, J. Hao, and W. Liu, *J. Am. Chem. Soc.* **127**, 15670 (2005).

(51) E. Givenchy, S. Amigoni, C. Martin, G. Andrada, L. Caillier S. Geribaldi, and F. Guittard, *Langmuir* **25**, 6448 (2009).

(52) K. Tadanaga, N. Katata, and T. Minami, *J. Am. Ceram. Soc.* **80**, 1040 (1997).

(53) W. Wu, X. Wang, X. Liu, and F. Zhou, *Appl. Mater. &Interface* **8**, 1656

(2009)

(54) K. Liao, A. Wan, J. D. Batteas, and D. E. Bergbreiter, *Langmuir* **24**, 4245 (2008).

(55) H. M. Shang, Y. Wang, S. J. Limmer, T. P. Chou, and K. Takahashi, G. Cao, *Thin Solid Films* **472**, 37 (2005).

(56) M. Hikita, K. Tanaka, T. Nakamura, T. Kajiyama, and A. Takahara, *Langmuir* **21***,* 7299 (2005).

(57) T. Ameri, G. Dennler, C. Lungenschmied, and C. J. Brabec, *Energy Environ. Sci.* **2**, 347 (2009).

(58) J. Nelson, *Science* **293**, 1059 (2001).

(59) C. J. Brabec, S. Sariciftci, and J. C. Hummelen, *Adv. Func. Mater.* **11**, 15 (2001).

(60) J. Li, and A. C. Grimsdale, *Chem. Soc. Rev.* **39**, 2399 (2010).

(61) P. W. M. Blom, V. D. Mihailetchi, L. J. A. Koster, and D. E. Markov, *Adv. Mater.* **19**, 1551 (2007).

(62) C. Deibel, and V. Dyakonov, *Rep. Prog. Phys.* **73**, 096401 (2010).

(63) G. Hodes, *J. Phys. Chem. C.* **112**, 17779 (2008).

(64) H. Hoppe, and N. S. Sariciftci, *J. Mater. Res.* **19**, 1924 (2004).

(65) Y. Zhou, M. Eck. And M. Kruger, *Energy Environ. Sci.* **3**, 1851 (2010).

(66) A. Shah, P. Tscharner, N. Wyrsch, and H. Keppner, *Science* **285**, 692 (1999).

(67) B. Walker, C. Kim, and T. Nguyen, *Chem. Mater.* **23**, 470 (2011).

(68) A. W. Hains, Z. Liang, M. A. Woodhouse, and B. A. Gregg, *Chem. Rev.* **110**, 6689 (2010).

(69) H. Ma, H. Yip, F. Huang, and A. K. Y. Jen, *Adv. Func. Mater.* **20**, 1371 (2010).

(70) W. U. Huynh, J. J. Dittmer, and A. P. Alivisatos, *Science* **295**, 5564 (2002).

(71) Y. Li, Q. Guo, Z. Li, J. Pei, and W. Tian, *Energy Environ. Sci.* **3**, 1427 (2010).

(72) I. Radivojevic, A. Varotto, C. Farley, and C. M. Drain, *Energy Environ. Sci.* **3**, 1897 (2010).

(73) J. Nelson, S. A. Choulis, and J. R. Durrant, *Thin Solid Films* **451**, 508 (2004).

(74) S. Uchida, J. Xue, B. P. Rand, and S. R. Forrest, *Appl. Phys. Lett.* **84**, 4218 (2004).

(75) V. D. Mihailetchi, H. Xie, B. Boer, L. J. A. Koster, and P W. M. Blom, *Adv. Func. Mater.* **16**, 699 (2006).

Chapter 3

3.1 Direct Method of Tracing the Wetting States on Nanocomposite Surfaces

PAPER 1: A Direct Method of Tracing the Wetting States on Nanocomposite Surfaces, **Langmuir** *26*, 7686 (2010).

Kevin K. Wang,[1] Han Yan,[1] Cindy X. Zhao,[1] Gu Xu,*,[1] Yu Qi,[2] Yiliang Wu,[2] Nan-Xing Hu[2]

[1] Department of Materials Science & Engineering, McMaster University, Hamilton, Ontario, L8S 4L7, Canada

[2] Xerox Research Center of Canada, Mississauga, Ontario, L5K 2L1, Canada

*AUTHOR EMAIL ADDRESS: xugu@mcmaster.ca

ABSTRACT: Identifying the two distinctive wetting states on a nanostructured surface remains an open challenge. We report here a direct method of tracing the Wenzel and Cassie states by using Ag nanoparticles as tracing agents. The method provides an answer to the long standing question of, whether there is a transition from Wenzel to Cassie state in the sliding angle drop, on superhydrophobic nanocomposite thin films containing multiwall carbon nanotubes.

3.1.1 Introduction

Superhydrophobic nanocomposite thin films are of special interests to the materials-research community due to their emerging applications, such as lossless transport of liquid drops,[1] antisticking structure of microelectromechanical systems (MEMS),[2] antisticking fuser roll in xerography,[3] self-cleaning thin films[4-6] and waterproof/ anti-icing coatings.[7-9] Commonly featured by a large water contact angle (CA), and reduced sliding angle (SA), defined to be the critical angle when a water droplet begins to slide down on a tilted plane,[10] the origin of superhydrophobicity of nanocomposites is usually analyzed by the so called Wenzel model which relates the contact angle to the surface roughness, versus Cassie model that concerns with the contact area fraction versus solid-liquid interaction.[11,12] These models describe two distinctive wetting behaviors of a water droplet. In the Wenzel case, a water droplet completely wets the surface in spite of the existence of grooves, pits and pop-ups, leading to an intimate liquid-solid contact. On the contrary, in the Cassie state, there is trapping air in the grooves and pits, therefore the area of contacts is reduced to cover only the top parts of the protruding elements, and becomes much smaller than the apparent water-solid interface. In addition, these models serve the basis of more sophisticated models, such as the pillar model where the contact angle is related to the number density and the aspect ratio of simplified geometry represented by pillars, and the fractal model where the contact angle is determined by fractal dimension and the upper/lower limit lengths of the fractals, all involving Wenzel/Cassie states as the starting point of the analysis.[13-16]

In principle, whether the contact is of Wenzel or Cassie case can be determined by the combine analysis of the two models,[17] where the transition from Wenzel to Cassie state occurs when the contact angle reaches a critical value, θ^*. However, they cannot be deducted by the critical contact angle calculated from the combine analysis of the two models, due to the fact that the fraction of contact area of liquid-solid interface (Φs) is difficult to measure and surface roughness (r) cannot be determined accurately on the nanoscale. For example, using visible light reflection to magnify the apparent water-solid interface,[18,19] direct observation of the Cassie state is only possible for a water droplet sitting on a surface structure of micrometer scale or greater. The technique cannot be duplicated on a nanoscale, due simply to the diffraction limit of the visible light. This limit could somewhat be pushed by scanning electron microscopy (SEM), for example, the wetting behavior of a water droplet on micro-protrusions of a lotus leaf was identified by Chen et al using environmental scanning electron microscopy (ESEM),[20] and the Cassie state for a water droplet on an area of 1 μm^2 was also observed by magnetic alternating current-mode atomic force microscopy.[20] In general, it is challenging to resolve the cases involving nanopits of 100 nm diameter or less. In particular, there remains a long standing question of, whether the transition from the Wenzel to Cassie state exists during the sliding angle change found in many nanocomposite thin films.[21-24]

Related to the contact angle hysteresis, sliding angle is often determined by the dynamic factors such as the triple phase contact line in superhydrophobic nanocomposites.[21-24] Literature shows that,[10,25-33] while the contact angle usually varies slowly by the composition change, the accompanying sliding angle often drops sharply from 90° to less than 5° at a certain composition. One of the explanations of the phenomenon was given by Miwa et al, where no transition from the Wenzel to Cassie state was suggested.[27] The hypothesis of the Cassie state for water droplet during the entire process of sharp sliding angle drop, however, contradicts the results of Sheng et al, which assumed a Wenzel state before the sliding angle drop.[27-28] Although the transition of Wenzel to Cassie state was included by Sheng et al, the contact angle obtained from the experiments before the transition seems to fit the Cassie, rather than the desired Wenzel state.[28] On the other hand, Latthe et al believe that the sharp drop of the sliding angle has nothing to do with the transition from the Wenzel to Cassie state, but through the loading variation of silane, fluorine, or siloxane.[29-31] This may obviously be rejected by the fact that the composites without fluorine/silane/siloxane also have the same sharp sliding angle drop,[10,32-33] as observed by Jin et al,[32] Wang et al[10] and Zhao et al.[33]

To resolve these issues, in this report the direct observation of the Wenzel and Cassie states is achieved, of a water droplet sitting on a nanostructure surface of a superhydrophobic thin film. Both the Wenzel and Cassie states of a water droplet in the respective nanoscale pits of ca. 100nm diameter are directly observed by using Ag nanoparticles as tracing agents, dissolved in nitric acid solution used as a water substitute. For simplicity, we demonstrate the direct observation of the two states in two separate surfaces which is not synchronous with the sliding angle measurement. This is directly relevant to the situation where the two-states are produced by variable compositions. It may be possible to apply this method to the in situ transition of the single surface if the transition goes from Cassie to Wenzel state, as long as two separate SEM observations can be made before and after the transition.

Nevertheless, the method provides a solution to the long standing problem of whether there is a transition from Wenzel to Cassie state, found in sliding angle drop on superhydrophobic nanocomposite films with variable content of multiwall carbon nanotubes (CNT).

3.1.2 Experimental

The nanostructured thin film was fabricated by multi-wall carbon nanotubes (CNTs, diameter: 10-20nm, length: dozens of microns) and perfluoroalkoxy resin (PFA) (DuPont^{TM}Teflon$^{@}$ TE-7224) via spray coating. A PFA- polyacrylic acid (M_w=17000, Aldrich) modified CNT aqueous dispersion was obtained by simply mixing modified CNT and PFA in various ratio. The superhydrophobic coatings were prepared by spraying the dispersion onto a silicon wafer followed by curing.

The morphology and structure feature of the composite were characterized by scanning electron microscopy (JEOL-7000). The contact angle and the sliding angle were acquired by optical goniometer (DAT 1100 FIBRO for contact angle and DataPhysics OCA 20 for sliding angle). Deionized water (4μL) was placed on the thin film by microsyringe for contact angle and sliding angle measurement. The average contact angles were obtained by averaging the contact angle from eight different points.

3.1.3 Results and Discussion

The method employed here involves soluble nanoparticles, which should have little effect on the surface energy of the thin film, to be dispersed on the surface to trace the wetting/non-wetting states in three steps, as shown in

Scheme 3.1(a – f). First of all, tracing nanoparticles are carried into the nanopits by an organic agent which wets all parts of the surface as shown in Scheme 3.1(a - c). This is followed by the elimination of surfactant on the nanoparticles by physical and chemical methods shown in Scheme 3.1(d1 and d2), respectively. Second, the water droplet is replaced by a liquid of similar surface energy, but with the ability to dissolve the nanoparticles as shown in Scheme 3.1(e). Finally, the Wenzel state is identified by the absence of the dissolved nanoparticles which were etched by the liquid, using in situ SEM as shown in Scheme 3.1(f1); and the Cassie state is demonstrated by the observation of the remaining nanoparticles which were not touched by the liquid, due to the presence of air bubbles, as shown in Scheme 3.1(f2).

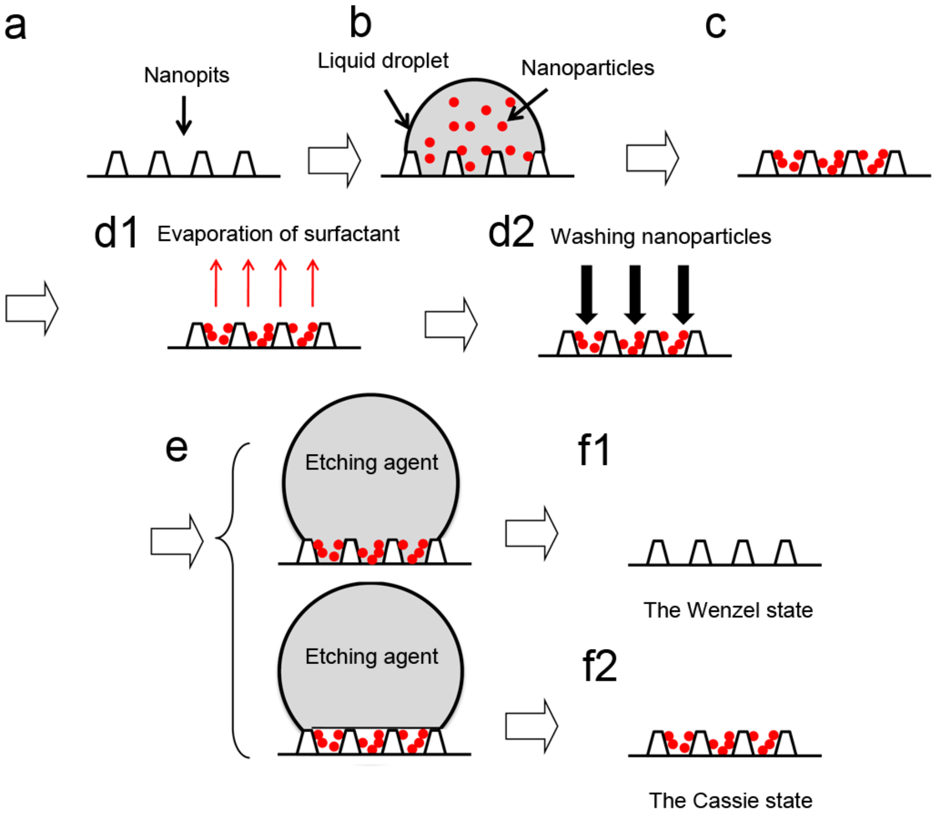

Scheme 3.1: **(**a) Nanostructured surface, where the valleys represent nanopits. (b) Organic agent containing tracing nanoparticles on the surface. (c) Dispersed nanoparticles on the surface. (d1) Physical method of eliminating the surfactant. (d2) Eliminating surfactant by the chemical method. (e) The Wenzel state, nanoparticles are etched by the acid droplet leading to (f1); The Cassie state, the nanoparticles are not touched, resulting in (f2).

Obviously, one needs to choose the right nanoparticles, which are to be well dispersed and dissolved by a proper substitute of water. Among the choices, the stability and the dissolubility of nanoparticles are important considerations, for the SEM observation of the nanoparticles before and after etching. The metal oxide nanoparticles cannot be a suitable candidate, due to the possible agglomeration in organic solution led by strong attraction of the hydroxyl group on the surface, or difficulty to remove the surfactant.[34-36] For metallic nanoparticles, only Ag or Au nanoparticles are stable enough to be used as tracing nanoparticles without the need of surfactant in room temperature.[37,38] Compared to Au nanoparticles, Ag nanoparticles in the size of 10nm can be well dispersed by 1-dodecyl-amine and are soluble in 2.2 M (mol L^{-1}) nitric acid solution, which has a surface energy of 71.9 mN/m (25 ℃), very similar to 71.99 mN/m (25 ℃) of water.[39] The preparation of Ag nanoparticles was described elsewhere.[40] Moreover, the necessary adhesion between Ag nanoparticles and surface of the nanocomposite film is formed after curing the film with Ag nanoparticles at 100 ℃, due primary to the low melting point of Ag nanoparticles. This adhesion is stronger than that between the usual surfactant and the film, which is beneficial to the fixing of the Ag nanoparticles. Therefore, the 10 nm Ag nanoparticles were found to be the best choice for the tracers.

The proposed method has been employed to study the question of whether there exists a transition from Wenzel to Cassie states when the sliding angle changes dramatically, which was found in many nanocomposite thin films.[27-33] The superhydrophobic nanocomposite containing CNTs used here is resistant to HNO_3, due to the presence of perfluoroalkoxy resins (PFA), which cover the CNT networks. The randomly located nanopores (ca. 100nm in diameter) of the superhydrophobic nanocomposite with a 30 wt% CNT loading are examined by scanning electron microscopy (SEM) (Fig. 3.1). As shown in Fig. 3.2, the sliding angle drops sharply whereas the contact angle varies slowly for a typical superhydrophobic nanocomposite containing variable CNT.[27-33]

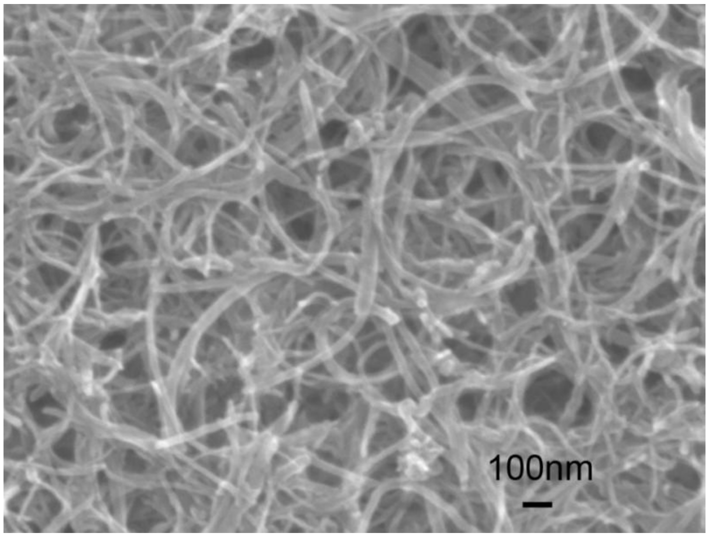

Figure 3.1: SEM image showing nanopores in the size of 100 nm.

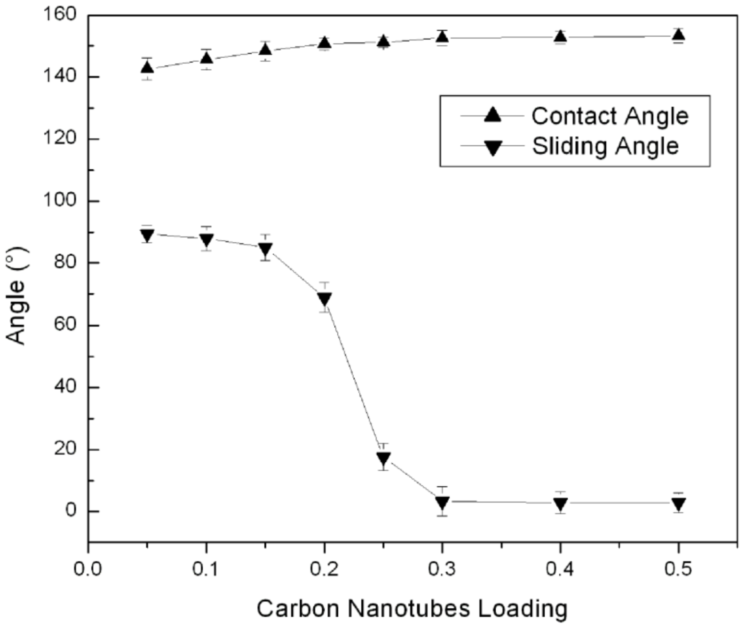

Figure 3.2: The sliding angle and contact angle change on a superhydrophobic nanocomposite thin film with a variable CNT content.

To verify whether the nitric acid can be used as water substitute for the CNT-PFA thin films, the contact angles of water and 2.2 M nitric acid solution were studied on nanocomposite thin films containing 10 wt% and 30 wt% carbon nanotubes, respectively. As shown in Fig. 3.3(a) and (b), the contact angles of water and nitric acid solution are almost identical. In Fig. 3.3(c) and (d), the contact angles of water and nitric acid solution are changed slightly by 1.0% and 1.3%, respectively, which suggests that the Ag nanoparticles have little effect on the superhydrophobicity of the nanocomposite thin film with 30wt% CNT. Similarly, Fig. 3.3(e) and (f) show that the wetting behavior of nitric acid solution is the same as that of water on the film with 10wt% CNT; also Ag nanoparticles have little effect on the superhydrophobicity of the 10wt% CNT film, as shown in Fig 3.3(g) and (h). All these confirm that it is possible to use 2.2 M nitric acid solution to replace water, in determining the wetting behavior of a water droplet with the surface of a superhydrophobic nanocomposite thin film containing carbon nanotubes.

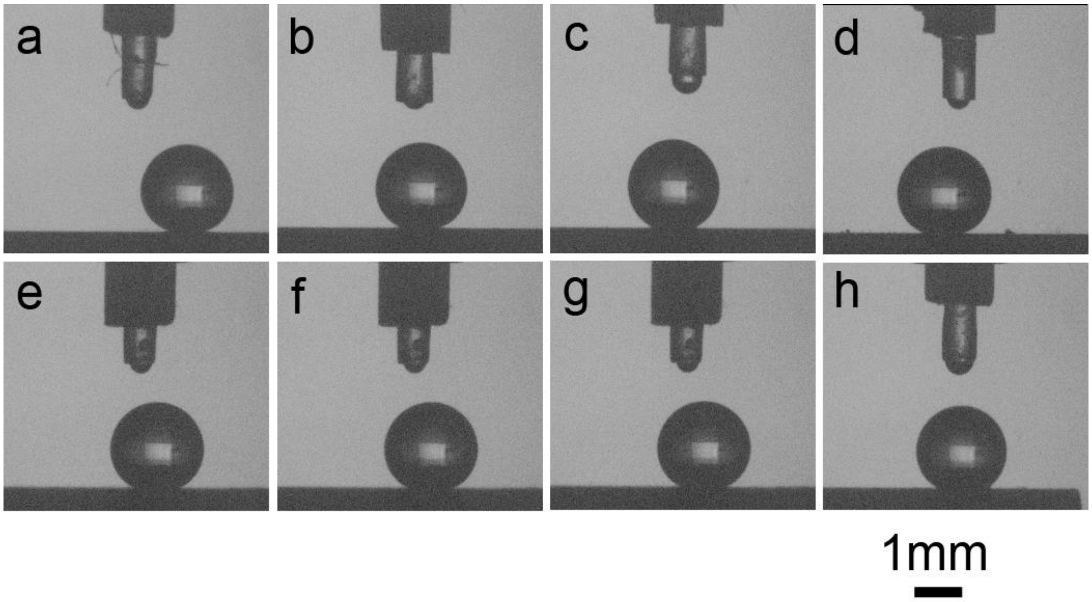

Figure 3.3: a) Water droplet on 30 wt% CNT surface with a contact angle of 153.5 ± 1.5°. b) HNO_3 on 30 wt% CNT surface with a contact angle of 152.2 ± 2.4°. c) Water droplet on the 30 wt% CNT surface with Ag with a contact angle of 152.0 ± 1.1°. d) HNO_3 on the 30 wt% CNT surface with Ag with a contact angle of 151.5 ± 1.0°. e) Water droplet on 10 wt% CNT surface with a contact angle of 145.6 ± 1.0°. f) HNO_3 on 10 wt% CNT surface with a contact angle of 145.3 ± 0.9°. g) Water droplet on the 10 wt% CNT surface with Ag with a contact angle of 145.9 ± 1.8°. h) HNO_3 on the 10 wt% CNT surface with Ag with a contact angle of 144.1 ± 0.9°.

The method is then applied as follows: the Ag nanoparticles dissolved in toluene (contact angle: 32.5 ± 0.7°) of 0.025 wt% concentration were dispersed into the nanopits of the nanocomposites. Next, the film with Ag nanoparticles was baked in a 100 ℃ oven for 1 hour, followed by washing with 5mL 0.1 M acetic acid in toluene to eliminate the surfactant. The Ag nanoparticles of 10 nm size were found to be well dispersed on the surface containing 10 wt% and 30 wt% CNT as shown in Fig. 3.4(a) and (c), respectively. Finally, a droplet of 2.2 M nitric acid of 4 µL was placed on the films for 3 minutes before removal. Through SEM observation, the Wenzel state of the water in the 100 nm nanopits is identified by the dissolved Ag nanoparticles at the same location indicated by the arrows as shown in Fig. 3.4(b). Therefore, the Wenzel state of water is demonstrated when the sliding angle is 90°, giving by the nanocomposite thin film of 10 wt% CNT loading. On the other hand, the Cassie state is demonstrated by the remaining Ag nanoparticles which were not touched by the acid, again using SEM when the sliding angle is 2.3°, obtained from a film of 30 wt% CNT as shown in Fig. 3.4(d). Therefore the transition from Wenzel to Cassie state of water droplet is finally confirmed accompanied by the sliding angle change.

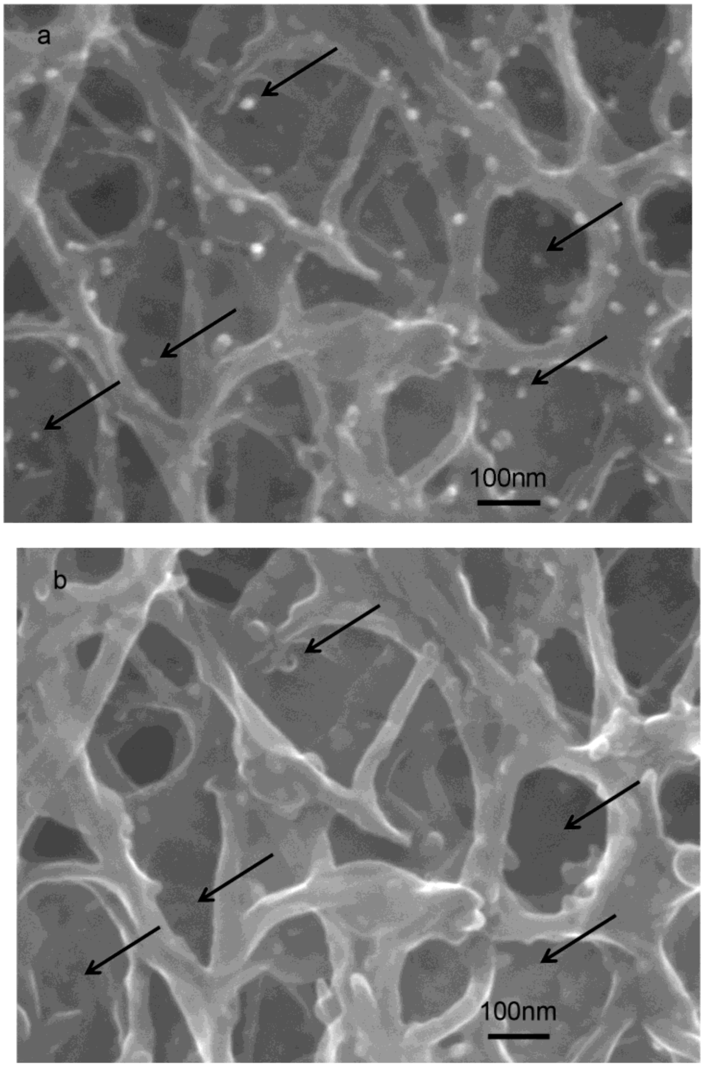

Figure 3.4: a) Nanocomposite containing 10 wt% CNT dispersed with Ag nanoparticles before etching, the white dots are Ag nanoparticles indicated by the arrows. b) In the same location as a), the 10 wt% CNT surface with Ag nanoparticles after etching, all the Ag nanoparticles indicated by the arrows were etched away, showing that the nitric acid droplet was in Wenzel state.

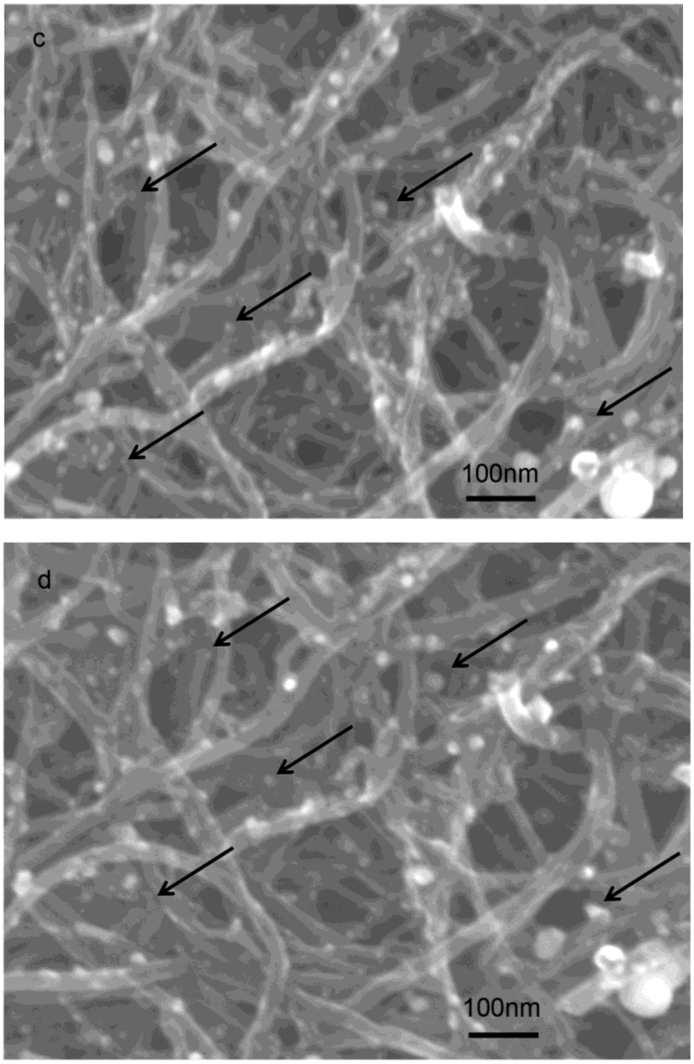

Figure 3.4: c) Nanocomposite containing 30 wt% CNT dispersed with Ag nanoparticles before etching, the white dots indicated by the arrows are the Ag nanoparticles in various nanopits. d) In the same location as c), the 30 wt% CNT surface with Ag after etching, all the Ag nanoparticles indicated by the arrows remains, showing that the nitric acid droplet was in Cassie state.

3.1.4 Conclusion

To summarize, a direct method is obtained to trace the Wenzel and Cassie states of a water droplet on the nanostructured surface of superhydrophobic nanocomposite thin films. Using Ag nanoparticles as tracing agent dissolved in nitric acid solution, Wenzel and Cassie states in nanopits are observed by SEM. The method provides a unique opportunity to identify the behavior of a water droplet on nanostructured surfaces, and thus enable the proper analysis for the superhydrophobic nanocomposite thin film. In particular, the determination of the Wenzel or Cassie state of a water droplet on CNT-PFA superhydrophobic nanocomposite thin film has been accomplished, to answer the long standing question of, whether the transition from Wenzel to Cassie state exists in the sliding angle change found in many nanocomposite thin films.

References

(1) X. Hong, X. Gao, and L. Jiang, *J. Am. Chem. Soc.* **129** (6), 1478 (2007).

(2) Y. Xiu, L. Zhu, D. W. Hess, and C. P. Wong, *Nano Lett.* **7** (11), 3388 (2007).

(3) M. Satoh, T. Okami, and N. Shimamoto, Fuser Roll, U.S. Patent 5,547,742, (1994).

(4) X. Li, D. Reinhoudt, and M. Crego-Calama, *Chem. Soc. Rev.* **36** (8), 1350 (2007).

(5) L. Feng, S. Li, Y. Li, H. Li, L. Zhang, J. Zhai, Y. Song, B. Liu, L. Jiang, and D. Zhu, *Adv. Mater.* **14** (24), 1857 (2002).

(6) R. Blossey, *Nature Mater. **2*** (5), 301 (2003).

(7) J. Genzer, and K. Efimenko, *Biofouling* **22** (5), 339 (2006).

(8) T. Kako, A. Nakajima, H. Irie, Z. Kato, K. Uematsu, T. Watanabe, and K. Hashimoto, *J. Mater. Sci.* **39** (2), 547 (2004).

(9) L. Zhai, F. C. Cebeci, R. E. Cohen, and M. F. Rubner, *Nano Lett.* **4** (7), 1349 (2004).

(10) Z. Wang, N. Koratkar, L. Ci, and P. M. Ajayan, *Appl. Phys. Lett.* **90** (14), 143117 (2007).

(11) R. N. Wenzel, *Ind. Eng. Chem.* **28**, 988 (1936).

(12) A. B. D. Cassie, and S. Baxter, *Trans. Faraday. Soc.* **40**, 546 (1944).

(13) N.A. Patankar, *Langmuir* **20** (19), 8209 (2004).

(14) N.APatankar, *Langmuir* **19** (4), 1249 (2003).

(15) T. Onda, S. Shibuichi, N. Satoh, and K. Tsujii, *Langmuir* **12** (9), 2125 (1996).

(16) S. Shibuichi, T. Onda, N. Satoh, and K. Tsujii, *J. Phys. Chem.* **100** (50), 19512 (1996).

(17) A. Lafuma, and D. Quere, *Nature Mater.* **2** (7), 457 (2003).

(18) M. Nosonovsky, and B. Bhushan, *Nano Lett.* **7** (9), 2633 (2007).

(19) C. Luo, X. Zuo, L. Wang, E. Wang, S. Song, J. Wang, J. Wang, C. Fan, and Y. Cao, *Nano Lett.* **8** (12), 4454 (2008).

(20) P. Chen, L. Chen, D. Han, J. Zhai, Y. Zheng, and L. Jiang, *Small* **5** (8), 908 (2009).

(21) L. Gao, and T. J. McCarthy, *Langmuir* **22** (7), 2966 (2006).

(22) D. Öner, and T. J. McCarthy, *Langmuir* **16** (20), 7777 (2000).

(23) E. Pierce, F. J. Carmona, and A. Amirfazli, *Colloids and Surfaces A: Physicochem. Eng. Aspects*, **323**, 73 (2008).

(24) W. Chen, A. Y. Fadeev, M. C. Hsieh, D. Öner, J. Youngblood, and T. J. McCarthy, *Langmuir* **15** (10), 3395 (1999).

(25) H. Y. Erbil, A. L. Demirel, Y. Avci, and O. Mert, *Science* **299**, 1377 (2003).

(26) S. Srinivasan, V. K. Praveen, R. Philip, and A. Ajayaghosh, *Angew. Chem. Int. Ed.* **47** (31), 5750 (2008).

(27) M. Miwa, A. Nakajima, A. Fujishima, K. Hashimoto, and T. Watanabe, *Langmuir* **16** (13), 5754 (2000).

(28) X. Sheng, and J. Zhang, *Langmuir* **25** (12), 6916 (2009).

(29) S. S. Latthe, H. Imai, V. Ganesan, and A. V. Rao, *Appl. Surf. Sci.* **256** (1), 217 (2009).

(30) N. Zhao, Q. Xie, X. Kuang, S. Wang, Y. Li, X. Lu, S. Tan, J. Shen, X. Zhang, Y. Zhang, J. Xu, and C. Han, *Adv. Funct. Mater.* **17** (15), 2739 (2007).

(31) Z. Cui, L. Yin, Q. Wang, J. Ding, and Q. Chen, *J. Colloid and Interface Sci.* **337**(2), 531 (2009).

(32) M. Jin, X. Feng, J. Xi, J. Zhai, K. Cho, L. Feng, and L. Jiang, *Macromol. Rapid Commun.* **26**, 1805 (2005).

(33) Y. Zhao, Q. Lu, D. Chen, and Y. Wei, *J. Mater. Chem.* **16** (46), 4504 (2006).

(34) L. Guo, S. Yang, C. Yang, P. Yu, J. Wang, W. Ge, and G. Wong, *Chem. Mater.* **12** (8), 2268 (2000).

(35) A. K. Gupta, and M. Gupta, *Biomaterials* **26** (18), 3995 (2005).

(36) N. Kohler, G. E. Fryxell, and M. Zhang, *J. Am. Chem. Soc.* **126** (23), 7206 (2004).

(37) R. R. Naik, S. J. Stringer, G. Agarwal, S. E. Jones, and M. O. Stone, *Nature Mater.* **1** (3), 169 (2002).

(38) Y. Sun, and Y. Xia, *Science* **298**, 2176 (2002).

(39) D. R. Lide, Handbook of Chemistry and Physics, 86th Ed.; CRC Press LLC; Boca Raton, FL, p 6-148 (2005).

(40) Y. Li, Y. Wu, and B. S. Ong, *J. Am. Chem. Soc.* **127**, 3266 (2005).

3.2 Stable Superhydrophobic Composite Coatings Made from an Aqueous Dispersion of Carbon Nanotubes and a Fluoropolymer

PAPER 2: Stable Superhydrophobic Composite Coatings Made from an Aqueous Dispersion of Carbon Nanotubes and a Fluoropolymer **Carbon** *49,* 1769 (2011).

Kewei Wang [2], Nan-Xing Hu [1], Gu Xu [2], Yu Qi [1,*]

[1] Xerox Research Centre of Canada 2660 Speakman Drive, Mississauga, Ontario, L5K 2L1, Canada

[2] Department of Materials Science & Engineering, McMaster University 1280 Main Street West, Hamilton, Ontario, L8S 4L7, Canada

*Corresponding author. E-mail address: yu.qi@xrcc.xeroxlabs.com

ABSTRACT: An easy method is reported for fabricating a stable superhydrophobic coating made from a composite comprising carbon nanotubes and a fluoroplastic such as polytetrafluoroethylene or perfluoroalkoxy resin (Teflon® PFA). The superhydrophobic coatings with hierarchical structure characteristics are fabricated by a spray coating technique using an environmentally friendly aqueous dispersion containing carbon nanotubes and perfluoroalkoxy resin. Coatings with a contact angle of 153.1 ± 2° and a sliding angle less than 5° are stable under much stress

conditions, i.e. either soaking in concentrated hydrochloric acid and concentrated sulfuric acid, or attacking with extreme-pH or ionic-strength solutions. Both the contact angle and sliding angle can be tuned simply by changing the carbon nanotube loading. To further the understanding of the formation of superhydrophobicity, we investigated both the formation of the nano/ microscale structures and their effects.

3.2.1 Introduction

Superhydrophobic phenomenon, observed from lotus leaf and water striders, is of special interest to the material-research community due to its potential applications.[1-3] Superhydrophobic surfaces have both water contact angles larger than 150º and sliding angles smaller than 5º. Both materials with low surface energy and surface morphology with hierarchical structures are essential for forming superhydrophobicity.[4-6] The common strategy of many fabrication methods, such as template replication,[7,8] lithography,[9,10] plasma treatment,[11] and vapor deposition,[12-14] is to manipulate the surface morphology to achieve superhydrophobicity. On the other hand, in order to simplify the preparation method, nano- and micro-materials have been synthesized, including crystalline inorganic materials,[15,16] polystyrene microspheres,[17,18] grafted nanotubes and microfibers,[19,20] to achieve the desired surface morphology. However, it still remains a considerable challenge to fabricate superhydrophobic surfaces using a widely applied industrial process.

For their applications, superhydrophobic coatings are often required to be stable under various conditions. For example, the superhydrophobic coatings used for microfluidic chips need to be tolerant to biologically relevant agents such as ionic buffer solutions, proteins and nucleic acids,[21-23] and the superhydrophobic coatings applied in radar antennas, airplanes, and power lines should be weathering resistant.[24,25] Recently, carbon nanotubes (CNTs) are introduced to fabricate superhydrophobic surfaces for the chemical stability and the ability of forming nanostructures. Lau et al. in 2003 reported that the surface of carbon nanotube forests, which are coated with polytetrafluoroethylene using enhanced chemical vapor deposition, exhibit remarkable superhydrophobicity.[26] However, the enhanced chemical vapor deposition cannot be used as an industrial process. Since then, more materials with CNTs for fabricating the superhydrophobic surface have been developed, such as the CNTs composite coatings prepared by solvent casting using the chloroform solution containing conjugated polymer-treated CNTs, such as olig(p-phenylenevinylene)s-graft[27] or poly(3-hexylthiophene)-block-polystyrene (rrP3HT-b-PS)-graft CNTs,[28] and by spray-coating a fluorinated sol-gel solution containing silica nanoparticles and oxidized CNTs.[29] Nevertheless, the olig(p-phenylenevinylene), rrP3HT-b-PS, and silica nanoparticles are not stable under weather conditions. It still remains a challenge to reach the required stability of superhydrophobic surfaces under various stress conditions using a widely applied industrial process.

Here we report an easy method for fabricating stable superhydrophobic coatings that are made from a composite comprising CNTs and a fluoroplastic such as polytetrafluoroethylene or perfluoroalkoxy resin (Teflon® PFA). As both CNTs and fluoroplastics are chemically inert materials, the composite coatings exhibit remarkable resistance to various stress conditions, such as strong acids and UV radiation. The superhydrophobic coatings with hierarchical structure characteristics are fabricated by a spray coating technique using an environmentally friendly aqueous dispersion containing CNTs and perfluoroalkoxy resin (Teflon® PFA). Both the contact angle and sliding angle can be tuned simply by changing the CNT loading. To further the understanding of the formation of superhydrophobicity, we investigated both the formation of the nano/ microscale structures and their effects.

3.2.2 Experimental

CNT were purchased from Cheap Tubes Inc. (diameter: 10-20nm, length: dozens of microns) and used as received. Perfluoroalkoxy resin (PFA) (60 wt%) and Poly (acrylic acid) (PAA) (Mw=17000) were purchased from DuPont Inc. and Aldrich, respectively. 1wt% CNT were well dispersed in water with 1.1wt% PAA after sonicating for 45min. CNT/PFA dispersion was prepared by mixing modified CNT and PFA in different ratio. The superhydrophobic coatings were fabricated by spraying the dispersion containing 5g CNT dispersion and 0.083g PFA latex onto silicon wafer followed by baking the coating in oven at 350°C for 30 minute and cooling down to room temperature. The thickness of the coating 7-10 μm is measured by length gauge (Heidenhain MT60M).

The intensity of the ultraviolet light used in the experiment is 1 $W \cdot cm^{-2}$ (wavelength: 250-360nm). The morphology and structure feature of the composite were characterized by SEM (JEOL-7000), AFM (Nanoscope III), and optical profilometer (Nanovea ST400). The contact angle and the sliding angle were acquired by optical goniometer (DAT 1100 FIBRO for contact angle and DataPhysics OCA 20 for sliding angle). Deionized water (4μL) was placed on the coating by microsyringe for contact angle measurement. The average contact angles were obtained by averaging the contact angle from eight different points.

3.2.3 Results and Discussion

To achieve a stable coating from an aqueous dispersion, it is critical to select the right surfactant that is able to disperse and stabilize CNTs in water, allow the resulting CNT dispersion compatible with the PFA latex, and can be removed thermally from the final coatings as any residual hydrophilic surfactant affects the stability of superhydrophbicity. There are many surfactants available to stabilize CNTs in the aqueous media, e.g. polyethyleneimine, gum arabic, polyallylamine hydrochloride, PEDOT:PSS and poly(acrylic acid) (PAA). Among these, polyethyleneimine and gum arabic are ruled out due to inability to make the CNT dispersion compatible with the PFA latex. Furthermore, although polyallylamine hydrochloride and PEDOT:PSS lead to good dispersion of CNTs/PFA, they are difficult to be removed from the final coatings. Finally, Poly (acrylic acid) (PAA) is the only one that meets all the requirements. PAA is not only capable of ensure a long shelf life of the coating dispersion (> 6 months), but is removable from the coating after baking above the melting temperature of PFA as its degradation temperature (about 200°C) is much lower than the melting temperature of PFA (310°C). We, therefore, prepared the composite coatings by making an aqueous coating dispersion containing PFA and CNTs that was stabilized by PAA, followed by depositing the dispersion on a substrate using a spray coating technique, and then baked the coating at an appropriate temperature (e.g. 330°C-350°C) to form a continuous film. A typically resulted coating, such as the one containing 50 wt% CNTs and 50 wt% PFA, displays superhydrophobic behavior at the surface with the water contact angle (CA) of 153.1 ± 2° and the sliding angle of less than 5°.

The superhydrophobic surface derived from the CNTs/PFA composite coating is extremely stable even under much stress conditions, i.e. either soaking in concentrated hydrochloric acid and concentrated sulfuric acid, or attacking with extreme-pH or ionic-strength solutions. To demonstrate the stability of the superhydrophobic composite coatings, we conducted a series of CA measurement on the coating samples of 50 wt% CNTs under various conditions. The measured CA had no substantial change before and after 24-hour soaking in concentrated hydrochloric acid (153.5° vs. 151.2°) and in concentrated sulfuric acid (153.4° vs.150.8°) as shown in Fig. 3.5(a-b) and (d-e). Long-time exposure to ultraviolet radiation did not affect the CA (Fig. 3.5c and 3.5f), and the CA measured before and after were 152.5° and 153.6°, respectively. The CA remained unchanged not only for water (Fig. 3.5g) but also for solutions with various pH values (Fig. 3.5h). The effect of ionic strength was evaluated by measuring the CA with different concentrations of NaCl solutions as the media. As shown in Fig. 3.5i, the CA remained the same even when the concentration of NaCl solutions increased. As a comparison, although the composite coatings made with poly(allylamine) hydrochloride as the dispersant displayed the same superhydrophobicity as the coatings prepared from PAA formulation, the contact angle of the coating is less than 90° after soaking in concentrated hydrochloric acid or concentrated sulfuric acid.

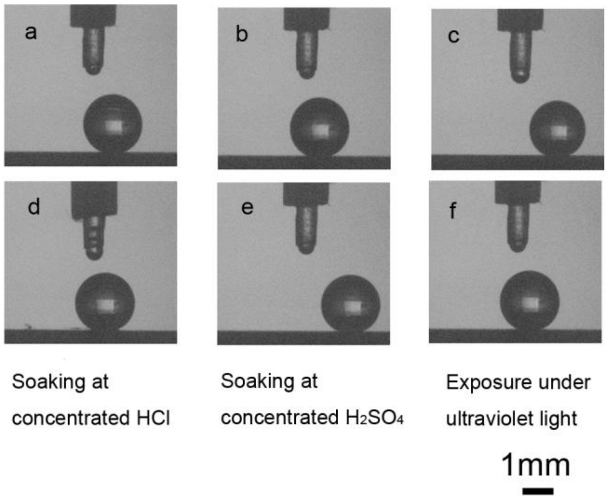

Soaking at concentrated HCl

Soaking at concentrated H_2SO_4

Exposure under ultraviolet light

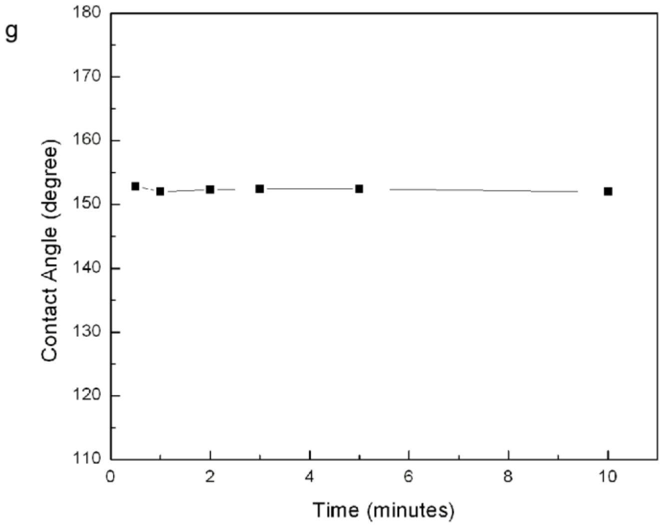

Figure 3.5: (a) - (f) Digital images of the contact angles before and after soaking in the solutions of concentrated hydrochloric acid or concentrated sulfuric acid, and exposure to ultraviolet light. (g) The contact angles against time.

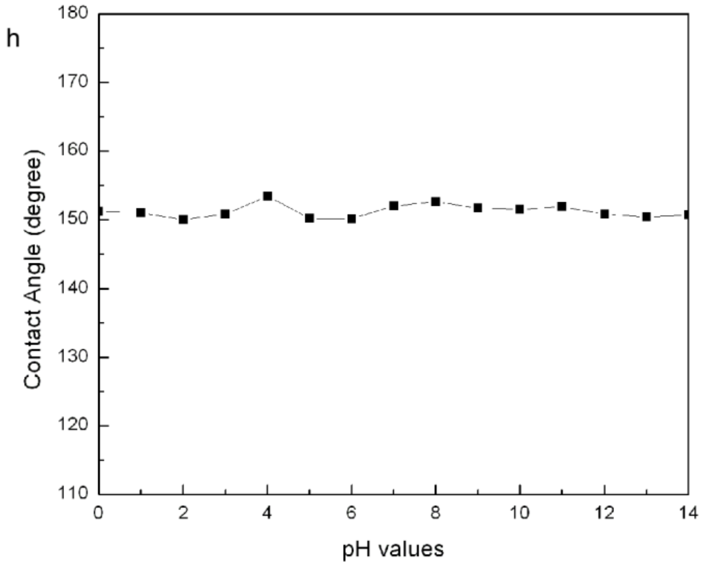

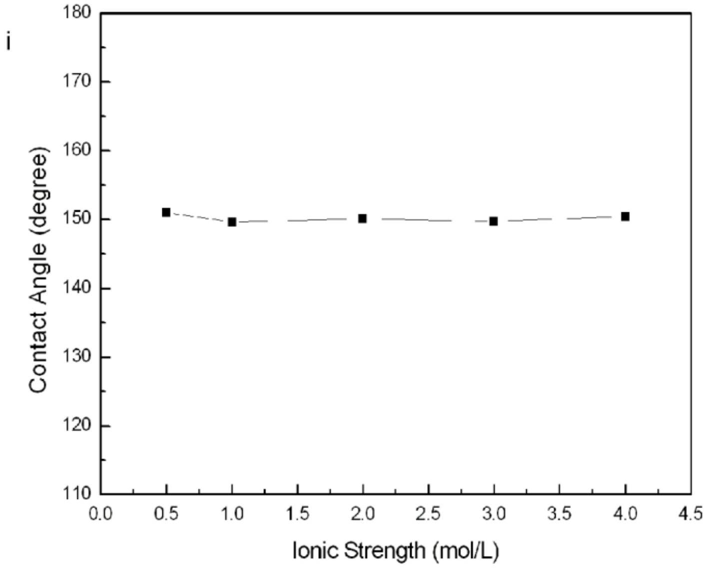

Figure 3.5: (h) The contact angles as the function of pH value. (i) The effect of NaCl ionic strength on the contact angles.

To achieve the superhydrophobicity with the CNTs/PFA composite coatings, it is critical to obtain hierarchical structures consisting of nano and micro roughness. The nanostructure prevents the condensation of nanodroplets, whereas the microstructure hinders the capillary wave penetration.[30-32] To understand the relationship between the surface morphology and the superhydrophobicity, and how the morphology is modulated by tuning the material composition, both micro and nanostructures of the coating were examined using the scanning electron microscopy (SEM), the atomic force microscopy (AFM), and the optical profilometry.

To study the effect of nanoscale roughness on the superhydrophobicity, we monitored how the contact angle is affected by the CNT loading in the composite coatings. When the CNT loading was increased from 0 to 5 wt%, and 30 wt%, the contact angles rose from 110.4° to 142.2°, and 153.1° (Fig. 3.6a). The AFM results reveal that with the increase of the CNT loading, the root-mean-square roughness of the nanostructure ($S_{q\text{-}n}$) increased from 4.41 nm to 33.13 nm, and 54.18 nm when the microscale roughness remained at 0.55-0.65 μm. The AFM image shows that the averaged nano-size hill-and-valley height increased from 20-30 nm for the pure PFA coating (Fig. 3.9a in Supplementary data) to 200 nm for 5 wt% CNTs (Fig. 3.9b in Supplementary data), and 300 nm for the 30 wt% CNTs (Fig. 3.9c in Supplementary data). Thus, this enhancement of the nanoscale roughness contributes significantly to the increase of CA.

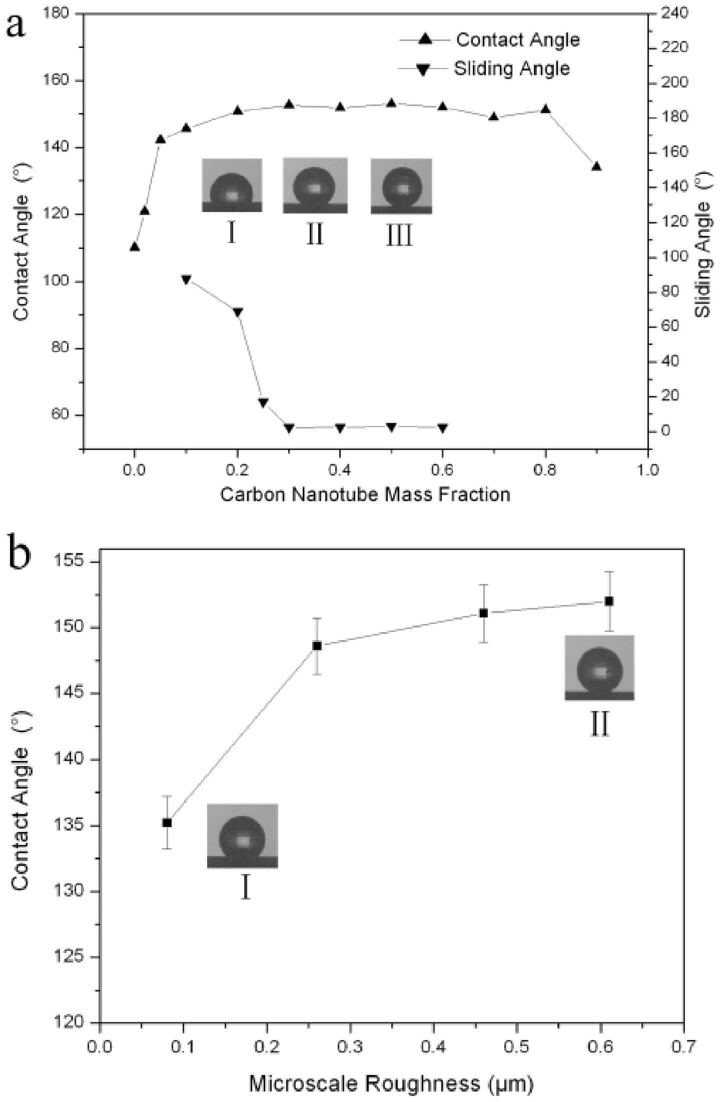

Figure 3.6: (a) The contact angle and sliding angle as a function of CNT loading (I: no CNT loading, Sq-n = 4.41 nm; II: 5 wt% CNT loading, Sq-n = 33.13 nm; III: 30 wt% CNT loading, Sq-n = 54.18 nm). (b) The contact angle as a function of microscale root mean square of composite surface.

The contact angle increased sharply even at low CNT loading, i.e., it reached 142.2° at 5 wt% CNT loading. In addition to the contact angle, the sliding angle is more responsive to the CNT loading. At the CNT loading of 5 wt%, the water drop pinned on the surface at any tilted angle. As the CNT loading was increased to 30 wt%, the sliding angle decreased dramatically to the rolling state (< 5°). The SEM image shows that the density of the nanopits significantly grew with the increase of the CNT loading, i.e. from 5 wt% (Fig. 3.7b) to 30 wt% (Fig. 3.7c). Although the nanopits formed at the CNT loading of 5 wt% (compared to the pure PFA coating (Fig. 3.7a)), the density was not enough to lower the sliding angle. The CNT loading brings about both the formation of nanopits and the growth of nanopits density, which in turn modulates both the contact and sliding angles. Thus, the surface property of the composite coating can be simply determined by the CNT loading. For example, the surface feature changes from the rose-like (high CA and high SA)[33] to lotus-like (high CA and very low SA)[34] as the CNT loading changes from 5 wt% to 30 wt%.

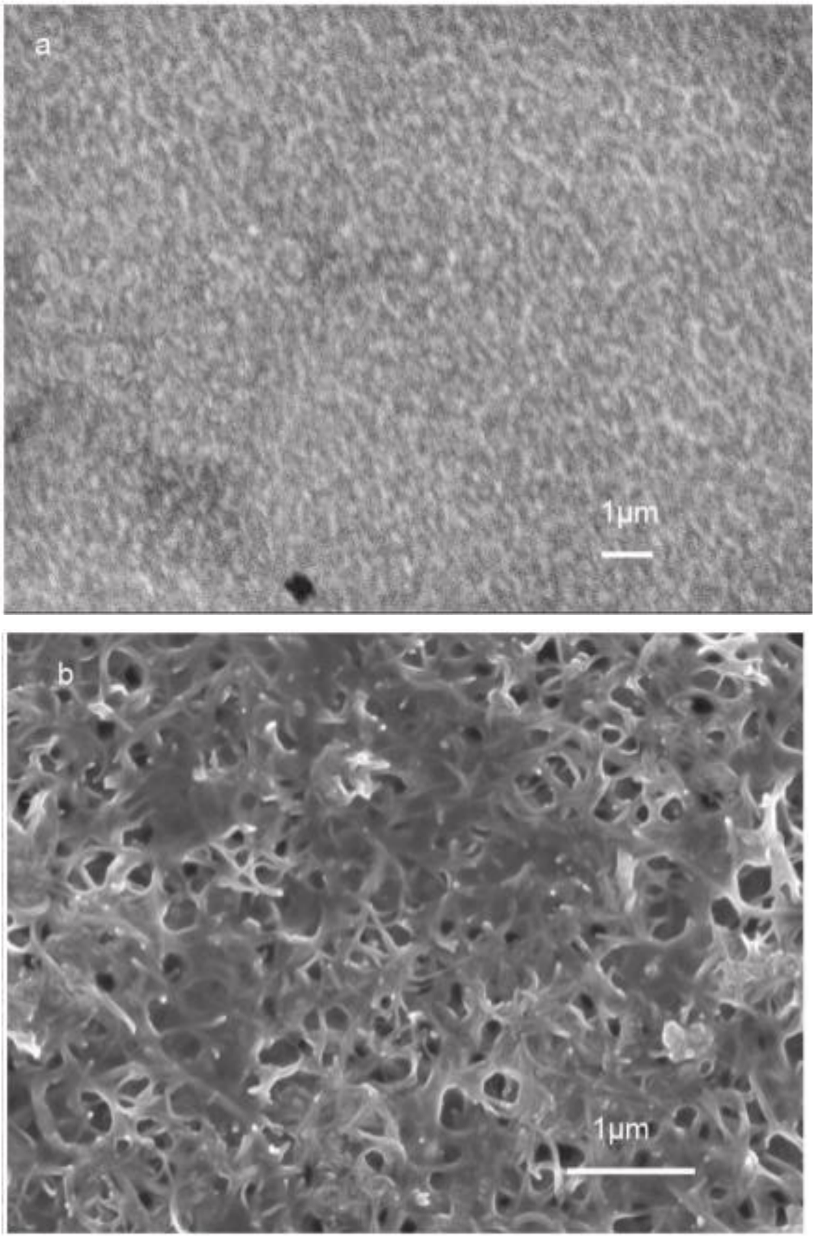

Figure 3.7: (a) The SEM image showing that no nanopits were observed at the pure PFA surface. (b) The SEM image of the 5 wt% CNTs-95 wt% PFA coating with nanopits.

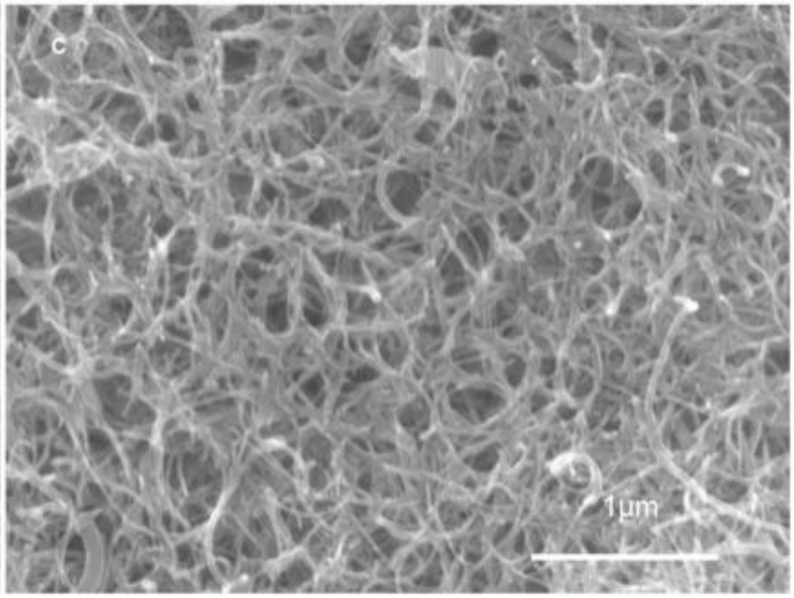

Figure 3.7: (c) The SEM image of the 30 wt% CNTs-70 wt% PFA coating with the high nanopits density.

To investigate why the superhydrophobicity is also attributed to the microscale roughness, a series of coatings containing 50 wt% CNTs were prepared with various microscale roughness by modulating the coating thickness. The contact angles of the composite coatings were presented as a function of microscale root-mean-square ($S_{q\text{-}m}$) obtained from the optical profilometry analysis (Fig 3.6b). When the microscale roughness was low, the coating surface did not reach the surperhydrophobic stage even at the high CNT loading. The contact angle became 152.0º when the roughness was increased to 0.61 µm, whereas it was only 135.2º when the microscale roughness was 0.08 µm (Fig. 3.6b). The microscale roughness can be characterized by the special features of microbumps on the surface.

To investigate the formation of the microbumps, we compared the composite coating to either the pure PFA coating or the pure CNT coating, and examined several factors, such as the substrate type, coating parameter, and CNT loading degree. The results show that neither the pure PFA coating nor the pure CNT coating was able to form microbumps (Figure 3.10 in Supplementary data). Moreover, the formation of the microbumps was not related to the substrate type, the spray coating parameters (such as the spray-gun nozzle size and spray speed), and CNT loadings. The results also show that the formation of the microbumps was determined by the nature of the aqueous coating dispersion of PFA and PAA-modified CNTs, and particularly caused by the aggregation of PFA nanoparticles. The SEM images exhibit that the as-sprayed coating surface had PFA nanoparticle aggregates, which formed microbumps after baking with the temperature above the PFA melting point (Fig. 3.8a-d). It is assumed that when water evaporates from the PFA nanoparticle aqueous dispersion during the spay-coating, the aggregation occurs due to the hydrophobic nature of the PFA polymer. After baking at the temperature of 350 °C, neither the size nor the location of microbumps changed (Fig. 3.8c). The optical profilometry analysis shows that microbumps had the features of 50-70 μm in diameter, 3 μm in height, and 50-70 μm in between-bump distance (Fig. 3.8e). The hierarchical structure that is consisted of microbumps covered with nanopits (Fig. 3.8d), is similar to that of the lotus leaf surface (Fig. 3.8f).[30,34]

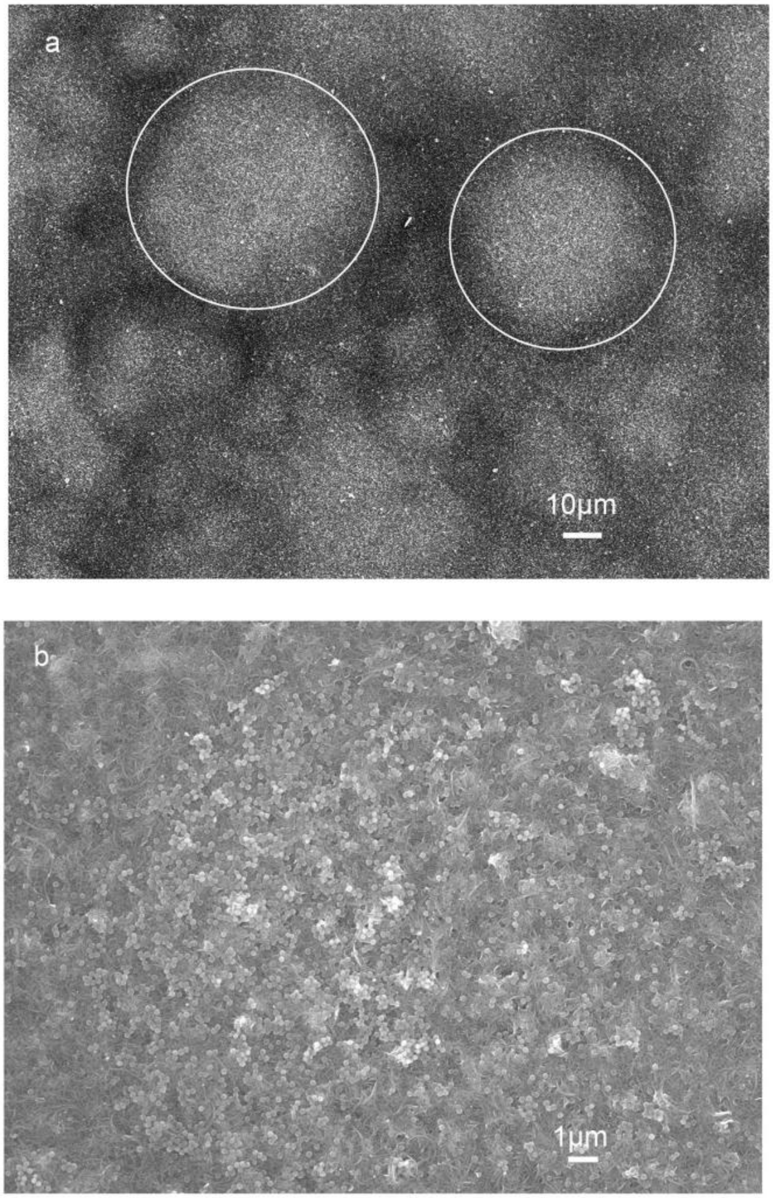

Figure 3.8: (a) The SEM image of the microbumps before baking. (b) The SEM image of PFA agglomeration before baking.

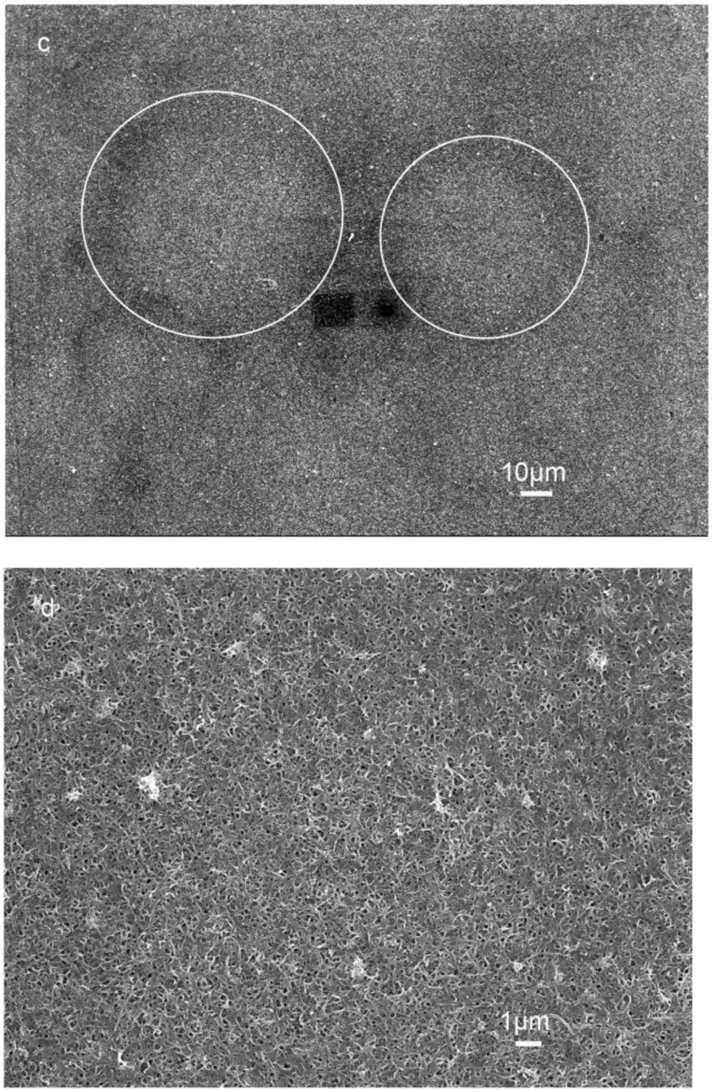

Figure 3.8: (c) The SEM image of the microbumps after baking. (d) The SEM image showing the formation of nanopits on the microbump after baking.

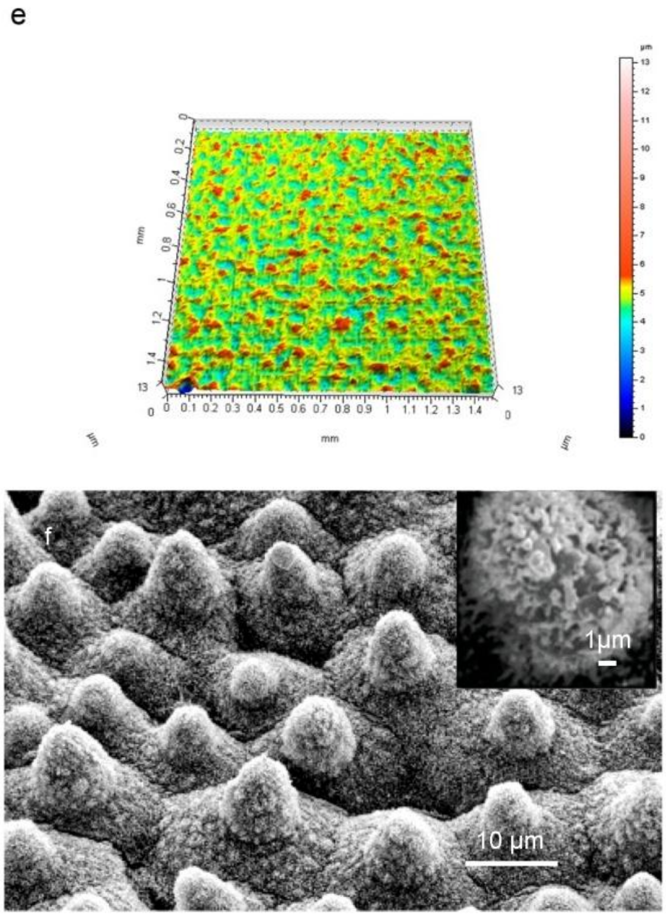

Figure 3.8: (e) The profilometry image of 50 wt% CNT coating. (f) The microstructure of lotus leaf. Inset, the nanostructure of the microbump surface of lotus leaf (Reproduced with permission from 30, 34. Copyright 2010 American Chemical Society. Copyright 2010 Wiley Interscience).

3.2.4 Conclusion

In conclusion, we developed CNTs/PFA composite coatings with the hierarchically structured superhydrophobic surface using an easy spray coating method. The hierarchical structure is consisted of PFA-covered nano-pits on micro-bumps. The superhydrophobic composite coating is stable under the stress conditions, such as soaking in concentrated hydrochloric acid or concentrated sulfuric acid, and exposure to ultraviolet light, high concentration of acid/base solution or liquid of high ionic strength. Both the contact angle and sliding angle can be tuned simply by changing the carbon nanotube loading. The formation of the microbumps was caused by the aggregation of PFA nanoparticles during the evaporation of the aqueous coating dispersion. The coating, with the advantages of the environmentally friendly material system, environmentally stable superhydrophobic surface, and easy application process, is potentially useful for industrial applications.

Supporting Information:

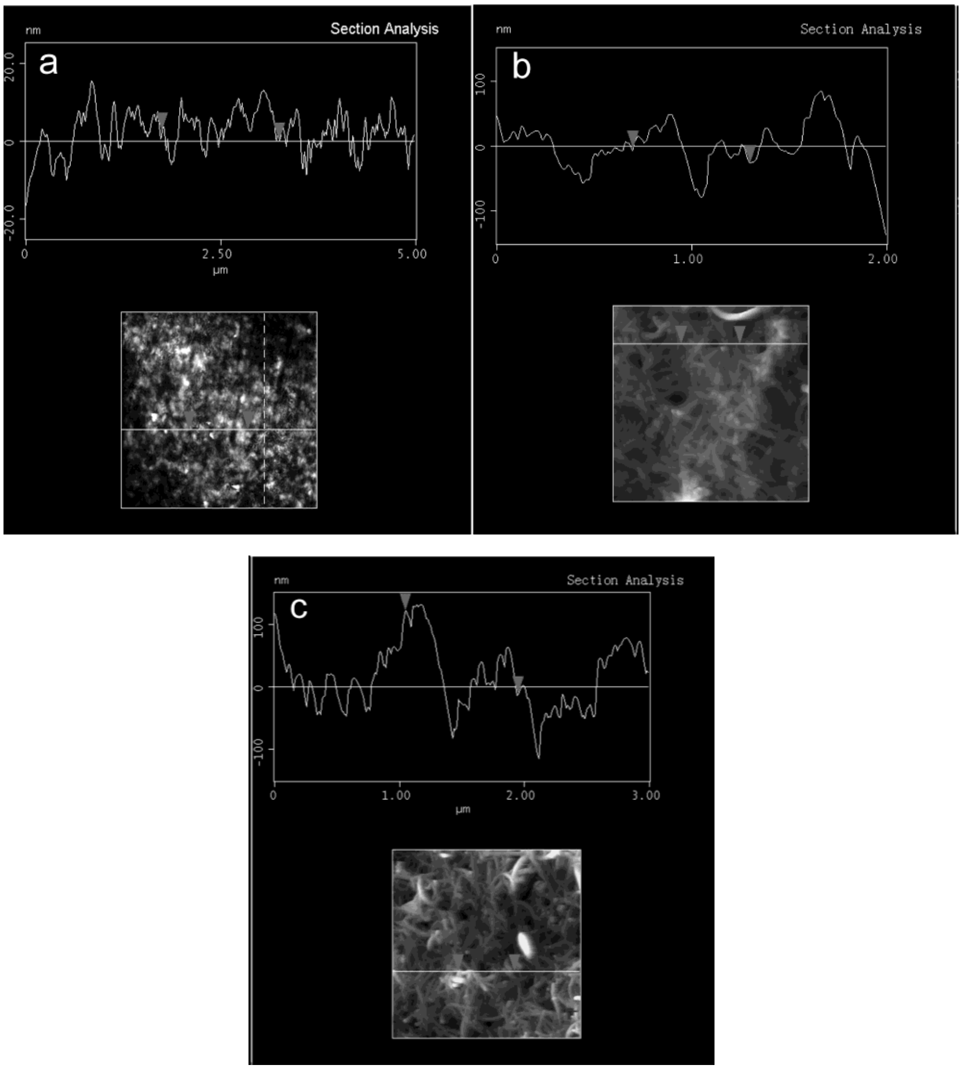

Figure 3.9: a) Height section analysis image of nanosized hills and valleys of pure PFA coating. b) Height section analysis image of nanosized hills and valleys of 5 wt% CNT-95 wt% PFA coating. c)Height section analysis image of nanosized hills and valleys of 30 wt% CNT-70 wt% PFA coating.

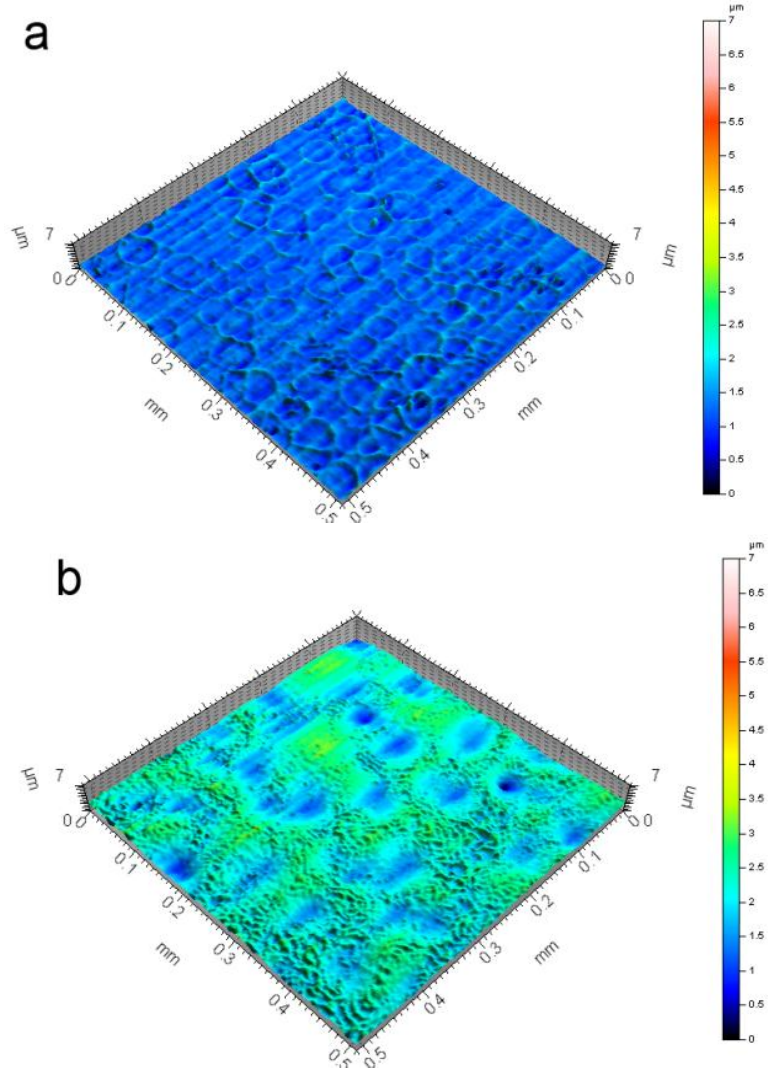

Figure 3.10: a) The profilometry image of pure PFA coating. b) Pure carbon nanotubes coating.

References

(1) X. Gao, and L. Jiang, *Nature* **432**, 36 (2004).

(2) H. Y. Erbil, A. L. Demirel, Y. Avci, and O. Mert, *Science* **299**, 1377 (2003).

(3) C.Neinhuis, and W. Barthlott, *Annals of Botany* **79** (6), 667 (1997).

(4) R. Blossey, *Nature Mater.* **2** (5), 301 (2003).

(5) M. Nosonovsky, and B. Bhushan, *Nano Lett.* **7** (9), 2633 (2007).

(6) X. Li, D. Reinhoudt, and M. Crego-Calama, *Chem. Soc. Rev.* **36**, 1350 (2007).

(7) W. Lee, M. Jin, W. Yoo, and J. Lee, *Langmuir* **20**, 7665 (2004).

(8) Y. Zhao, M. Li, Q. Lu, and Z. Shi, *Langmuir* **24** (21), 12651 (2008).

(9) M. Chen, T. Hsu, Y. Chuang, and F. Tseng, *Appl. Phys. Lett.* **95** (2), 023702 (2009).

(10) X. Huang, J. Lee, J. Lee, J. Yoon, and Y. Choi, *Small* **4**, 211 (2008).

(11) B. Cortese, S. D’Amone, M. Manca, I. Viola, R. Cingolani, and G. Gigli, *Langmuir* **24** (6), 2712 (2008).

(12) L. Zhai, F. C. Cebeci, R. E. Cohen, and M. F. Rubner, *Nano Lett.* **4** (7), 1349 (2004).

(13) M. Ma, Y. Mao, M. Gupta, K. K. Gleason, and G. C. Rutledge, *Macromolecules* **38**, 9742 (2005).

(14) Y. Xiu, L. Zhu, D. W. Hess, and C. P. Wong, *Nano Lett.* **7** (11), 3388 (2007).

(15) E. Hosono, S. Fujihara, I. Honma, and H. S. Zhou, *J. Am. Chem. Soc.* **127**,

13458 (2005).

(16) X. Wu, L. Zheng, and D. Wu, *Langmuir* **21**, 2665 (2007).

(17) Y. Li, X. Huang, S. H. Heo, C. Li, Y. Choi, W. Cai, and S. O. Cho, *Langmuir* **23***,* 2169 (2007).

(18) G. Zhang, D. Wang, Z. Gu, and H. Mohwwald, *Langmuir* **21**, 9143 (2005).

(19) K. Liao, A. Wan, D. Batteas, and J. D. E. Bergbreiter, *Langmuir* **24**, 4245 (2008).

(20) D. Nystrom, J. Lindqvist, E. Ostmark, P. Antoni, A. Carlmark, A. Hult, and E. Malmstrom, *ACS Appl. Mater. & Interfaces* **1**, 816 (2009).

(21) F. Mumm, A. T. J. Helvoort, and P. Sikorski, ACS *Nano* **3**, 2647 (2009).

(22) J. W. Hong, V. Studer, G. Hang, W. F. Anderson, and S. R. Quake, *Nature Biotechnology* **22**, 435 (2004).

(23) A. Egatz-Gomez, J. Schneider, P. Aella, D. Yang, P. Dominguez-Garcia, S. Lindsay, S. T. Picraux, M. A. Rubio, S. Melle, and M. A. A. Marquez, *Appl. Surf. Sci.* **254**, 330 (2007).

(24) J. Niu, J. Wang, and Q. Xu, *Langmuir* **24**, 6918 (2008).

(25) Z. Cui, L. Yin, Q. Wang, J. Ding, and Q. Chen, *J. Colloid & Interf. Sci.* **337**, 531 (2009).

(26) K. K. S. Lau, J. Bico, K. B. K. Teo, M. Chhowalla, G. A. J. Amaratunga, W. I. Milne, G. H. McKinley, and K. K. Gleason, *Nano Lett.* **3**, 1701 (2003).

(27) S. Srinivasan, V. K. Praveen, R. Philip, and A. Ajayaghosh, *Angew. Chem. Int. Ed.* **47**, 5750 (2008).

(28) J. Zou, H. Chen, A. Chunder, Y. Yu, Q. Huo, and L. Zhai, *Adv. Mater.* ***20***, 3337 (2008).

(29) J. T. Han, S. Y. Kim, J. S. Woo, and G. Lee, *Adv. Mater.* **20**, 3724 (2008).

(30) N. A. Patankar, *Langmuir* **20** (19), 8209 (2004).

(31) M. Nosonovsky, and B. Bhushan, *Microelectronic Engineering 84*, 382 (2007).

(32) M. Nosonovsky, *Langmuir* **23** (6), 3157 (2007).

(33) L. Feng, Y. Zhang, J. Xi, Y. Zhu, N. Wang, F. Xia, and L. Jiang, *Langmuir* **24**, 4114 (2008).

(34) F. Xia, and L. Jiang, *Adv. Mater*. **20**, 2842 (2008).

3.3 The Inverse Correlation between Series Resistance and Parallel Resistance of Small Molecule Organic Solar Cells

Manuscript Prepared

The Inverse Correlation between Series Resistance and Parallel Resistance of Small Molecule Organic Solar Cells

Kewei Wang,[1] Cindy X. Zhao,[1] Lucia L. Deng,[1] Yiqun Ma,[1] Richard A. Klenkler,[2] Hany Aziz,[3] Gu Xu[1]

[1]Department of Materials Science & Engineering, McMaster University, Hamilton, Ontario, L8S 4L7, Canada

[2]Xerox Research Center of Canada, Mississauga, Ontario, L5K 2L1, Canada

[3]Electrical and Computer Engineering, University of Waterloo, Waterloo, Ontario, N2L 3G1, Canada

ABSTRACT: Understanding the inversely correlated R_s and R_p remains a challenge. Here we report that the variation of R_s and R_p are inversely related through the morphology of the donor and acceptor interface in CuPc nanoparticle organic solar cells, when comparing the bilayer structure and bulk heterojunction structure. It is also found that the charge carrier concentration near the donor-acceptor interface plays an important role in the relationships of R_s and R_p under fixed interfacial morphology, which is verified by the change of V_{oc}. The inversely correlated R_s and R_p contribute to the improvement of the fill

factor, and in turn the PCE.

3.3.1 Introduction

Small-molecule organic solar cells have attracted growing attention in recent years because of their long term stability.[1-4] However, the common fabrication process involves costly vacuum evaporation, which limits their application.[5-7] Therefore, solution processing, has been proposed to replace the vacuum evaporation.[8-10] However, the usual solution process gives a much lower power conversion efficiency (PCE) than that from vacuum evaporation.[8-12]

A closer look at PCE indicates that it is related to open circuit voltage (V_{oc}), short circuit current (J_{sc}), and the fill factor, which is defined as the ratio of the maximum obtainable power to the product of J_{sc} and V_{oc}.[13-15] While V_{oc} is usually settled by the energy band gap of donor and acceptor materials, and the work function of the electrodes,[16,17] J_{sc} is largely determined by the interfacial area between donor and acceptor materials.[6-12] Describing the "squareness" of the current density-voltage (J-V) curve in the solar cell characterization, the fill factor is directly related to the series resistance (R_s), which is composed of bulk and interfacial resistances, and parallel resistance (R_p), which represents the electron-hole recombination at the donor-acceptor interface.[18] Apart from a lower J_{sc}, the fill factor is only 24%-41% in solution processed small molecule organic solar cells, much lower than, e.g., 60% from the vacuum evaporated case. [8-12] Therefore, the low fill factor becomes a critical issue to be addressed.

Ideally, R_s should be the lower the better, and R_p the higher the better.

However, with solution processed small molecule organic solar cells, R_s can be as high as 500Ω·cm^2 and accompanied by a low R_p of about 600Ω·cm^2, leading to a low fill factor and poor PCE.[8-10] Therefore, in order to improve the fill factor and thus the PCE of solution processed small molecule organic solar cells, it is crucial to understand the factors that determine the variation of R_s and R_p, and in particular, the correlation between R_s and R_p, if any.

From the equivalent circuit analysis, R_s and R_p are originally introduced as two separate elements. However, it is observed from literature that an increasing R_s is usually accompanied by a decreasing R_p and vice versa.[10,11,19-22] Therefore, it remains a challenging question of why R_s and R_p are inversely correlated and what is the underlying mechanism.

To answer the question, two methods were proposed here, to investigate the possible relationships between R_s and R_p. A comparison was made for the R_s and R_p values obtained from copper phthalocyanine (CuPc) nanoparticle based organic solar cells, with both bilayer and bulk heterojunction structures. The variation of R_s and R_p were found to be inversely related, through the morphology of the donor and acceptor interface. To further examine the correlation of R_s and R_p, the thickness of the CuPc layer in the bilayer organic solar cells was varied. It was found that the charge concentration near the donor-acceptor interface plays an important role in the relationships of R_s and R_p, which was further verified by the variation of V_{oc}.

3.3.2 Experimental

Both the bilayer and bulk heterojunction CuPc nanoparticle organic solar cells were fabricated on patterned indium tin oxide (ITO) substrates, with a sheet resistance of 15 $\Omega \cdot cm^{-2}$. A thin layer (30nm) of poly(3,4-ethylenedioxythiophene) : poly(styrenesulfonate) (PEDOT:PSS) was spin coated on top, and then baked at 120℃ for 10 minutes. A CuPc nanoparticle layer for the bilayer device, or a mixed layer consisting of CuPc nanoparticles and [6, 6']-phenyl-C61-butyric acid methyl easter (PCBM), with a weight ratio of 1:1 for bulk heterojunction device, were then spin coated on top of the PEDOT : PSS layer, followed by annealing the half prepared device at 200℃. Finally, a C_{60} (40nm) layer (only for the bilayer device), Bathocuproine (BCP) (10nm) and silver cathode (100nm) were thermally evaporated under a vacuum of $5*10^{-6}$ Torr. The overall device configuration thus becomes: ITO/ PEDOT:PSS/CuPc/C60/BCP/Ag for the bilayer devices; and: ITO/ PEDOT:PSS/CuPc:PCBM/BCP/Ag for the bulk heterojunction device. The R_s and R_p were calculated through the method reported elsewhere.[23]

The spin-coated CuPc layer was used for atomic force microscopy (AFM) imaging (Nanoscope), as shown in Fig.3.11. It is evident that the nanoparticles of about 20 nm in diameter and about 50 nm long are packed tightly, to form a thin film with root mean square roughness of 3.9nm. The crystallinity of the CuPc nanoparticles is greater than 80%, which gives a minimal grain boundary resistance.[24]

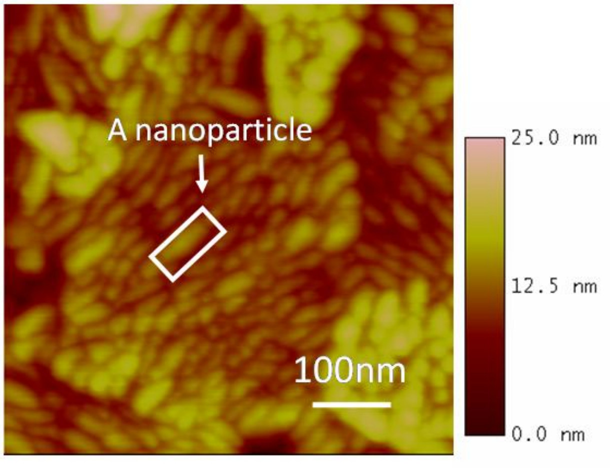

Figure 3.11: AFM image of the CuPc nanoparticle thin film.

3.3.3 Results and Discussion

To first confirm the literature observation that R_s and R_p are inversely correlated, CuPc nanoparticle based organic solar cells, with both bilayer and bulk heterojunction structures were fabricated to investigate the possible relationships between R_s and R_p. Since the bilayer-structured device has an activation layer of the same thickness, made of the same donor and acceptor molecules, as the bulk heterojunction device, the only difference between the two lies in the interfacial morphology of the activation layers. However, very different R_s and R_p values were obtained, as shown in Table 3.1. Compared to the bilayer device, a much larger R_s of $1060\Omega\cdot cm^2$, and a relatively lower R_p of $843\Omega\cdot cm^2$ were obtained from the bulk heterojunction device, resulting in a much poorer PCE. These results show an opposite trend between R_s and R_p, which has been reflected by the previous literature.[10,11,19-22]

TABLE 3.1: Photovoltaic parameters of the CuPc organic solar cells with bilayer and bulk heterojunction structures.

Device structure	PCE	V_{oc} (V)	J_{sc} (mA/cm^2)	Fill factor	R_s (Ω·cm^2)	R_p (Ω·cm^2)
Bulk heterojunction device	0.03%[‡]	0.218	0.5	27%	1060	843
Bilayer device	0.39%[‡]	0.376	2.0	52%	109	1280

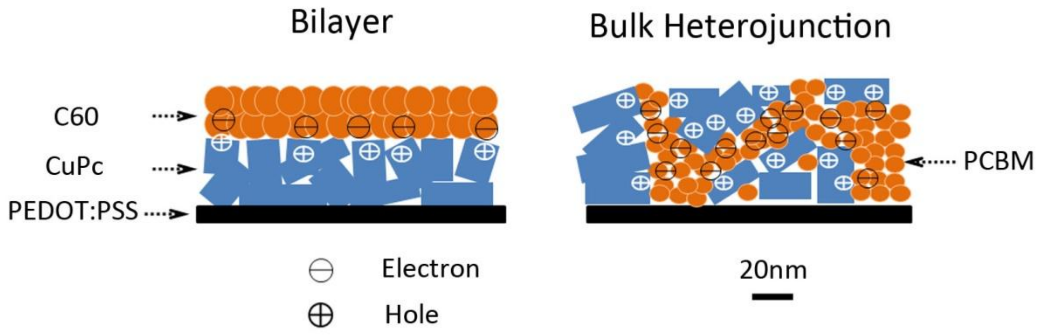

Scheme 3.2: The relationships between R_s and R_p in the CuPc nanoparticle organic solar cells with bilayer structure and bulk heterojunction structure

In order to understand the cause of the difference in R_s and R_p, an interfacial morphology model was proposed, as shown in Scheme 3.2. It is evident that, in the bilayer device, since the donor and acceptor were coated separately, all the donor/acceptor nanoparticles are well connected, creating

---

[‡] This is measured by a not-so-reliable light source. A correct value may be two times higher.

enough current paths for the charge carriers, thus leading to a low R_s. At the same time, as the total interfacial area of donor and acceptor is identical to the nominal area of the device, the electron-hole recombination at the interfacial area is low, resulting in a high R_p.

Conversely, in the bulk heterojunction device, as the CuPc and PCBM are mixed during fabrication, the donor/acceptor nanoparticles[25] may not be well connected with each other, or may even be isolated. Moreover, the donors are mostly surrounded by acceptor particles, and vice versa, leading to a much higher interfacial area of donor and acceptor than the nominal area of the device. Therefore, R_s is much larger than that of the bilayer device because of the poor hole/electron transport, while the R_p is lower due to the increase of the interfacial area.

It is thus demonstrated, that the R_s and R_p are inversely related, through the morphology of the donor and acceptor interface. The next question is, what happens under a fixed interfacial morphology.

To answer this question, the bilayer-structure was investigated, under a constant interfacial area of the donor and acceptor. Two experiments were performed: (1) varying the thickness of the CuPc layer, and (2) annealing the CuPc layer before the vacuum evaporation of C_{60}.

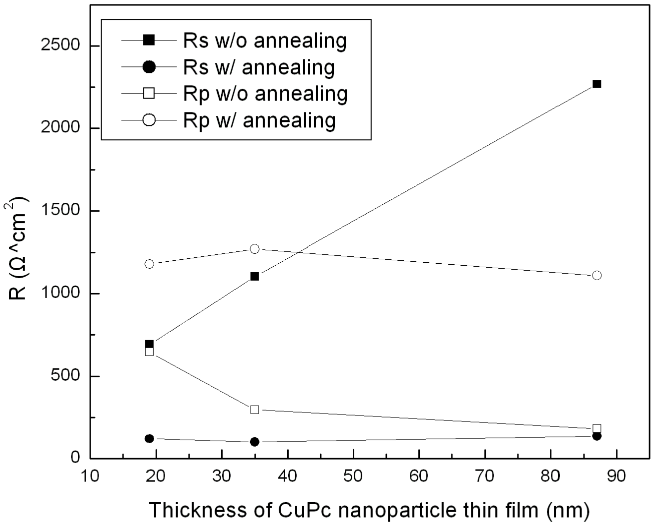

Figure 3.12: The R_s and R_p of the CuPc nanoparticle organic solar cells with different thickness of CuPc layer without and with annealing at 200℃.

As shown by Fig.3.12, before annealing, as the thickness of the CuPc layer is raised (from 19nm to 35nm and then to 87nm), R_s increases sharply, whereas R_p drops by more than a factor of 2. With annealing at 200℃, however, R_s drops from 692Ω·cm^2 to 121Ω·cm^2, while R_p rises from 647Ω·cm^2 to 1180Ω·cm^2. Therefore, the inverse correlation between R_s and R_p is maintained, even with the same interfacial morphology between the donor and acceptor.

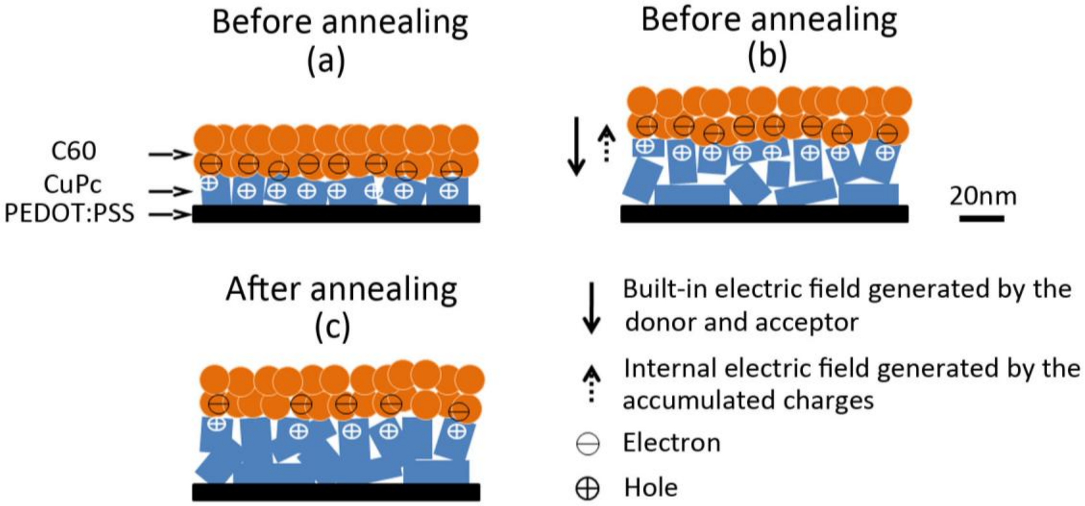

Scheme 3.3: The relation of R_s and R_p before and after annealing in bilayer- structured device.

To further analyze the possible cause of this inverse correlation, a second morphological model was proposed, as illustrated in Scheme 3.3. Before annealing (scheme 3.3a, 3.3b), since the CuPc nanoparticles are not well connected, the increased thickness introduces a large number of gaps among the CuPc nanoparticles, resulting in a poor charge transport, thus, a higher R_s. Meanwhile, charge carriers are accumulated, near the donor-acceptor interface. Therefore, the electron-hole recombination is boosted by the increased charge carrier concentration, resulting in a lower R_p.

After annealing, however, (scheme 3.3c), R_s drops, due to the formation of the nanosized current paths. This reduces charge accumulation, thus lower electron-hole recombination, and a higher R_p. Therefore, R_s and R_p are related each other, through the charge carrier concentration change, near the donor-acceptor interface, under a fixed interfacial area.

To further confirm the variation of the charge carrier concentration, near the donor-acceptor interface, the V_{oc} versus CuPc thickness was investigated. Analysis shows, (scheme 3.3b, 3.3c), upon the decrease of R_s after annealing, the charge carrier concentration near the donor-acceptor interface drops. Therefore, the internal electric field, generated by the accumulated charges, will also decrease. As a consequence, V_{oc} of the device should be improved, because the internal electric field generated by the accumulated charges is opposite to the built-in electric field by the donor and acceptor. The actual data shows that, before annealing, the V_{oc} was 0.297V, and R_s drops from 2269 $\Omega\cdot cm^2$ to 137$\Omega\cdot cm^2$, the V_{oc} increases to 0.350V after annealing at 200℃, due to the drop of accumulated charges. The same trend was also found in the device with the CuPc thickness of 35nm after annealing, where an increasing V_{oc} of 0.018V is achieved.

The very inverse correlation between R_s and R_p is actually favorable, since the decrease of R_s and the increase of R_p are both contributing to the improvement of the fill factor, and in turn the PCE, simultaneously. Fig.3.13 shows the J-V curve of the CuPc bilayer organic solar cells with and without annealing. After annealing at elevated temperatures, R_s drops from 1250 $\Omega\cdot cm^2$ without annealing, to 212$\Omega\cdot cm^2$ at 160℃, and finally reaches 85$\Omega\cdot cm^2$ at 200℃, whereas R_p is enhanced from only 186$\Omega\cdot cm^2$, to 1600$\Omega\cdot cm^2$, and then 3810$\Omega\cdot cm^2$, respectively. Both lead to an increased fill factor of 57%, which is 50% higher than the best reported result of the solution processed small molecule organic solar cells.[10] Correspondingly, the PCE of the devices is also improved from 0.01%[‡] to 0.45%[‡].

[‡] This is measured by a not-so-reliable light source. A correct value may be two times higher.

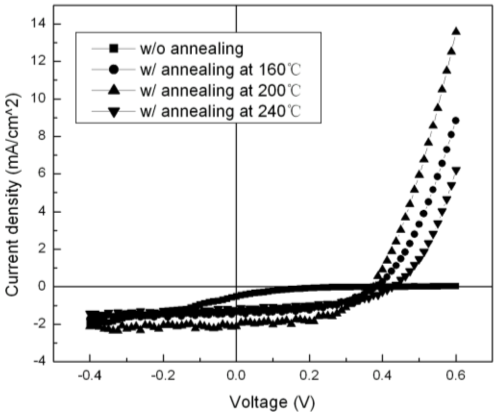

Figure 3.13: The J-V curves of the CuPc nanoparticle organic solar cells without and with annealing.

It should be noted, however, that the annealing cannot be overdone, as shown by the curve of 240℃ in Fig. 3.13, where the fill factor decreases slightly down to 48%. A possible cause is the poor contact between the CuPc layer and C_{60} layer, due to the growth of CuPc nanoparticles after over annealing.

3.3.4 Conclusion

To summarize, the variation of R_s and R_p are inversely related through the morphology of the donor and acceptor interface in CuPc nanoparticle organic solar cells, when comparing the bilayer structure and bulk heterojunction structure. By increasing the thickness of the CuPc layer in CuPc bilayer organic solar cells and characterizing the devices before and after annealing, it is found that R_s is also related to R_p through the charge carrier concentration, which is further confirmed by the variation of V_{oc}. The inverse relationship between R_s and R_p helps to improve the fill factor, and in turn the PCE.

References

(1) Y. Hsiao, W. Whang, S. Suen, J. Shiu, and C. Chen, *Nanotechnology* **19**, 415603 (2008).

(2) F. Liang, F. Shi, Y. Fu, L. Wang, X. Zhang, Z. Xie, and Z. Su, *Sol. Energy Mater. And Sol. Cells* **94**, 1803 (2010).

(3) C. Chu, V. Shrotriya, G. Li, and Y. Yang, *Appl. Phys. Lett.* **88**, 153504 (2006).

(4) J. Huang, J. Yu, H. Lin, and Y. Jiang, *J. Appl. Phys.* **105**, 073105 (2009).

(5) D. Gebeyehu, M. Pfeiffer, B. Maennig, J. Drechsel, A. Werner, and K. Leo, *Thin Solid Films* **451-452**, 29 (2004).

(6) N. Wang, J. Yu, Y. Zang, J Huang, and Y. Jiang, *Sol. Energy Mater. & Sol. Cells* **94**, 263 (2010).

(7) F. Yang, M. Shtein, and S. R. Forrest, *Nat. Mater.* **4**, 37 (2005).

(8) A. Varotto, C. Nam, I. Radivojevic, J. P. C. Tome, J. A. S. Cavaleiro, C. T. Black, and C. M.Drain, *J. Am. Chem. Soc.* **132**, 2552 (2010).

(9) A. Sanchez-Diaz, R. Pacios, U. Munecas, T. Torres, and E. Palomares, *Org. Electronics* **12**, 329 (2011).

(10) S. Schumann, R. A. Hatton, and T. S. Jones, *J. Phys. Chem. C* 115, 4916 (2011).

(11) J. Xue, B. P. Rand, S. Uchida, and S. R. Forrest, *Adv. Mater.* **17**, 66 (2005).

(12) P. Peumans, S. Uchida, S. R. Forrest, *Nat. Mater.* **425**, 158 (2003).

(13) J. Peet, J. Y. Kim, N. E. Coates, W. L. Ma, D. Moses, A. J. Heeger, and G. C. Bazan, *Nat. Mater.* **6**, 497 (2007).

(14) J. Y. Kim, K. Lee, N. E. Coates, D. Moses, T. Nguyen, M. Dante, and A. J. Heeger, *Science,* **317**, 222 (2007).

(15) H. X. Wei, J. Li, Z. Q. Xu, Y. Cai, J. X. Tang, and Y. Q. Li, *Appl. Phys. Lett.* **97**, 083302 (2010).

(16) C. J. Brabec, S. Sariciftci, and J. C. Hummelen, *Adv. Func. Mater.* **11**, 15 (2001).

(17) C. W. Schlenker and M. E. Thompson, *Chem. Commun.* **47**, 3702 (2011).

(18) R. A. Street, M. Schoendorf, *Phys. Rev. B* **81**, 205307 (2010).

(19) S. Yoo, B. Domercq, B. Kippelen, *Appl. Phys. Lett.* **85**, 5427 (2004).

(20) M. T. Lloyd, A. C. Tayi, A. M. Bowen, T. G. Kasen, D. J. Herman, D. A. Mourey, J. E. Anthony, and G. G. Malliaras, *Org. Electron.* **7**, 243 (2006).

(21) T. L. Chen, J. J. Chen, L. Catane, and B. Ma *Org. Electron.* **12**, 1126 (2011).

(22) M. Rusu, S. Wiesner, I. Lauemann, Ch. Fischer, K. Fostiropoulos, J. Audinot, Y. Fleming, M. Lux-Steiner, *Appl. Phys. Lett.* **97**, 073504 (2010).

(23) S. Choi, W. J. Potscavage Jr., and B. Kippelen, *J. Appl. Phys.* **106**, 054507 (2009).

(24) L. Deng, K. Wang, C. X. Zhao, H. Yan, J. F. Britten, and G. Xu, *Crystals*,

1, 112 (2011).

(25) M. T. Rispens, A. Meetsma, R. Rittberger, C. J. Brabec, N. S. Sariciftci, and J. C. Hummelen, *Chem. Commun.* **17** 2116 (2003).

3.4 High Fill Factor Solution Processed Copper Phthacyloanine Nanoparticle Organic Solar Cells

3.4.1 Experimental Details

The surfactant-free CuPc nanoparticles were prepared by dissolving 10mg CuPc in 20g concentrated H_2SO_4, followed by dropping CuPc - H_2SO_4 mixture into 700ml deionized water with constant stirring at 3ºC. Then, the nanoparticles obtained were washed with water and dried in a vacuum oven at 70ºC.

The structure of the CuPc nanoparticle organic solar cells is shown in Scheme 3.4. The organic solar cells were fabricated on patterned ITO substrates with a sheet resistance of 15 $\Omega\cdot cm^{-2}$. A thin layer (30nm) of PEDOT : PSS was spin coated on the top of ITO glass substrate, and then baked at 120 ℃ for 10 minutes. After the fabrication of a CuPc nanoparticle layer (≈20nm) by spin coating on top, the ITO/PEDOT : PSS/ CuPc layers were annealed at 200℃. Then the C_{60} (40nm) layer, Bathocuproine (BCP) (10nm) and silver cathode were thermally evaporated under a vacuum of $5*10^{-6}$ Torr.

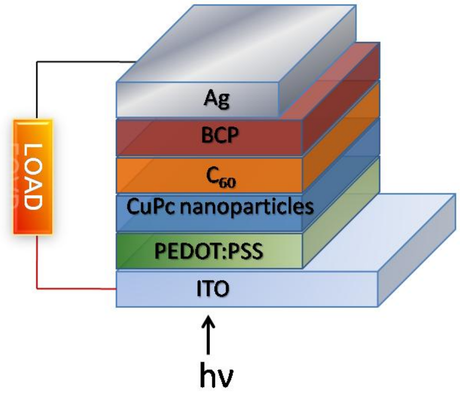

Scheme 3.4: The structure of CuPc nanoparticle organic solar cells.

3.4.2 Results and Discussion

Compared to the CuPc microsized particles, the size of CuPc nanoparticles are comparable to the exciton diffusion length, defined as the average distance an exciton can move from the point of generation until it recombines, implying productive exciton harvesting in the CuPc – C_{60} interface.[1] However, surfactants are usually applied in the synthesis of CuPc nanoparticles, which usually decrease the PCE of the CuPc organic solar cells and prevent the formation of CuPc/C_{60} interface.[2-4] Therefore, a new strategy is employed to precipitate CuPc - H_2SO_4 mixture directly into water, and to prepare the surfactant-free CuPc nanoparticles. The CuPc nanoparticle thin film made by the spin coating process was investigated by the UV-vis spectrum. As shown in Figure 3.14, the absorption peaks of CuPc nanoparticles are 326.5nm, 613.5nm and 700.5nm, which are similar to those of the CuPc as received.

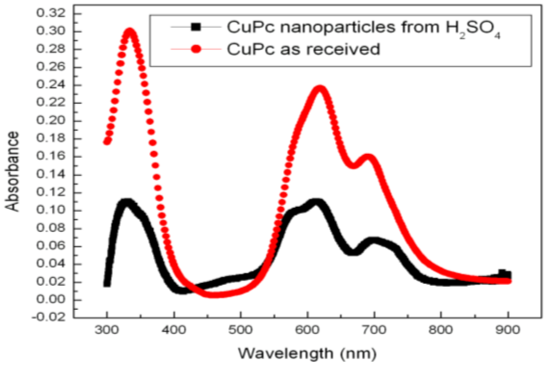

Figure 3.14: UV-vis spectrum of CuPc nanoparticles and CuPc bulk materials.

Based on these surfactant-free CuPc nanoparticles, the CuPc nanoparticle organic solar cells are fabricated by the spin coating process. The J-V curve in Figure 3.15 shows that the fill factor of the CuPc nanoparticle organic solar cells after annealing under 200 ℃ is as high as 58%, which is much higher than those of 24%-41%, reported in the literatures.[5-7]

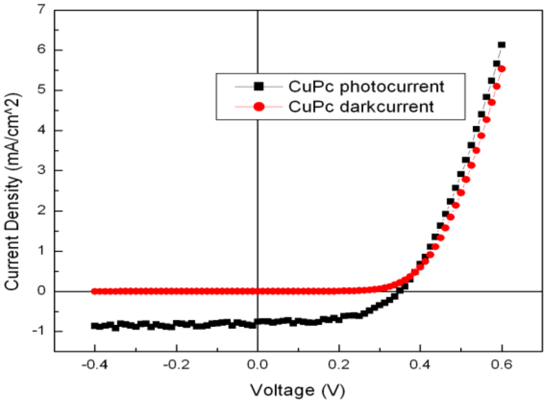

Figure 3.15: The current density- voltage curve of CuPc organic solar cells.

To elucidate the effect of annealing on the improvement of the fill factor, the series resistance and the parallel resistance of CuPc nanoparticle organic solar cells are investigated here. As shown in Table 3.2, after annealing, the R_s is reduced sharply from 1250 Ω ·cm^2 to 85Ω ·cm^2. At the same time, the R_p increases dramatically from 186Ω ·cm^2 to 3810 Ω ·cm^2. The decrease of R_s represents that the electrical contact of the device has been improved dramatically after annealing, and the improved electrical contact will contribute positively to the improvement of the fill factor. In the mean time, the enhancement of R_p shows that the probability of the recombination between electrons and holes is reduced. This also contributes to the improvement of the fill factor.

TABLE 3.2: Photovoltaic parameters of CuPc nanoparticle solar cells with various annealing temperature.

Annealing temperature (℃)	Fill factor	Voc (V)	Jsc (mA·cm^{-2})	Efficiency	Series resistance (R_s) (Ω·cm^2)	Parallel resistance (R_p) (Ω·cm^2)
W/o annealing	10%	0.383	0.87	0.01%‡	1250	186
160	53%	0.381	0.51	0.31%‡	212	1600
200	58%	0.348	0.76	0.47%‡	85	3810
240	48%	0.427	0.49	0.31%‡	238.5	2310

---

‡ This is measured by a not-so-reliable light source. A correct value may be two times higher.

During annealing, the nanosized current pathway is formed between nanoparticles, as shown in Scheme 3.5. Before annealing, the nanoparticles are not well connected, leading to a large series resistance. After annealing, the adjacent nanoparticles are connected by molecular diffusion. Therefore, the electrical conductivity between the nanoparticles is improved.

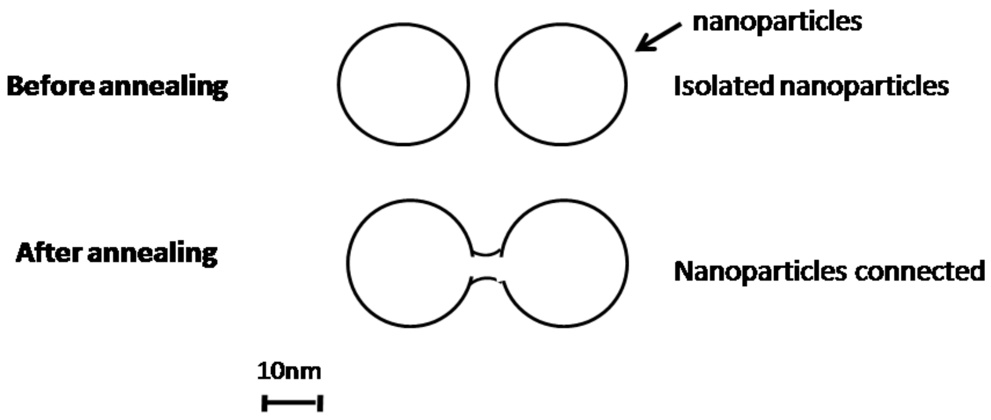

Scheme 3.5: The formation of nanosized current pathway.

However, the formation of nanosized pathway cannot be confirmed by the SEM image, because the size of the pathway is beyond the observing limitation of SEM, as shown in Figure 3.16.

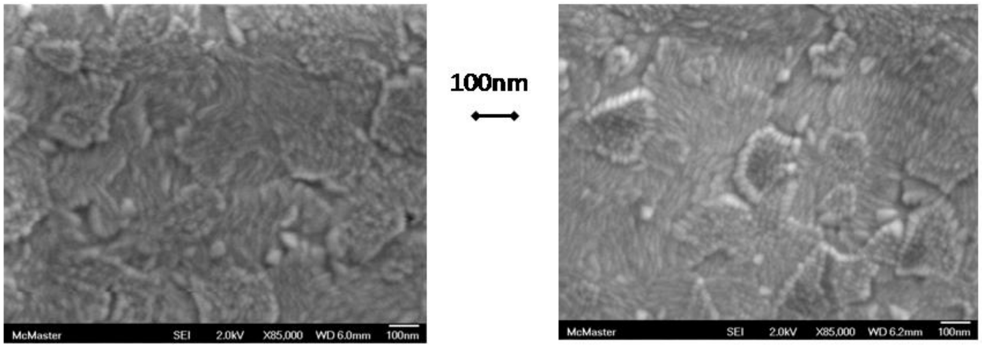

Before annealing **After annealing**

Figure 3.16: SEM images of CuPc nanoparticles before and after annealing at 200 ℃.

In conclusion, a surfactant-free CuPc small-molecule organic solar cell with high fill factor is developed by the spin coating method. The improvement of the fill factor is attributed to the formation of nanoscale current pathway between CuPc nanoparticles by annealing, which is proved by the decrease of series resistance and increase of parallel resistance.

Reference

(1) P. Peumans, A. Yakimov, and S. R. Forrest, *J. Appl. Phys.* **93**, 3693 (2003).

(2) Y. Wang, K. Deng, L. Gui, Y. Tang, J. Zhou, L. Cai, J. Qiu, D. Ren, and Y. Wang, *J. Colloid & Interface Sci.* **213**, 270 (1999).

(3) S. A. Jenekhe, and S Yi, *Adv. Mater.* **12**, 1274 (2000).

(4) Y. Wang, and D. Liang, *Adv. Mater.* **22**, 1521 (2010).

(5) A. Varotto, C. Nam, I. Radivojevic, J. P. C. Tome, J. A. S. Cavaleiro, C. T. Black, and C. M.Drain, *J. Am. Chem. Soc.* **132**, 2552 (2010).

(6) A. Sanchez-Diaz, R. Pacios, U. Munecas, T. Torres, and E. Palomares, *Org. Electronics* **12**, 329 (2011).

(7) S. Schumann, R. A. Hatton, and T. S. Jones, *J. Phys. Chem. C* 115, 4916 (2011).

Chapter 4 Summary and Conclusions

Overall, the findings and conclusions from the individual articles that make up this thesis have broad implications regarding the interfacial characteristics of nanomaterial-based composites and devices.

Although intensive research on the interfacial characteristics of nanomaterials has given us a deeper understanding, there are still some unexplored areas in the characterization, synthesis, and device application of nanomaterials, which were specified as follows: the difficulty in identifying the interfacial contacts of nanostructured surfaces, the instability of nanocomposite surfaces together with the complicated synthesis methods, and the under-researched mechanism of the correlation between interfacial characteristics and the performance of devices (e.g. organic solar cells).

Targeting the challenges mentioned above, the main theme of this thesis, therefore, is to investigate the interfacial contact of nanocomposites by direct observation, and to further develop a stable nanostructured surface based on which the direct observation can be conducted, and to eventually investigate the correlation between the interfacial contact and the performance of organic solar cells.

In order to indentify the wetting behaviors on a nanostructured surface, a direct method of tracing the two distinctive wetting states, the Cassie and Wenzel states, was developed, on nanostructured surfaces involving nanopits of 100nm or less, by using Ag nanoparticles as tracing agents and nitric acid as a water substitute. The method provided the answer to a long standing question of whether there is a transition from Wenzel to Cassie states in the sliding angle drop on nanostructured thin films. To accomplish the direct observation, a hierarchical structured superhydrophobic nanocomposite with excellent stability was fabricated by the spray coating method using an environmentally friendly aqueous dispersion containing multi-walled carbon nanotubes and PFA. The nanocomposites were stable under high stress conditions, such as, immersion in concentrated HCl and concentrated H_2SO_4, or attacked by solutions with extreme-pH or high ionic-strength. To further understand the formation of superhydrophobicity, the formation of nanostructures and microstructures, together with their effects were investigated.

Furthermore, in order to investigate the effect of interfacial contacts on the R_s and R_p in organic solar cells, a surfactant-free small-molecule nanoparticle organic solar cell with a much improved fill factor was developed. The inverse correlation between R_s and R_p was discovered in both bilayer structured and bulk-heterojunction structured small-molecule organic solar cells. The variation of R_s and R_p was determined by the morphology change of the donor and acceptor interface. It was also found that the charge concentration near the donor-acceptor interface plays an important role in the relationships between R_s and R_p under fixed interfacial morphology, which was verified by the variation of open circuit voltage. The inversely correlated R_s and R_p both improve the fill factor, and further enhance the power conversion efficiency.

These findings provide novel understanding in the area of nanomaterials. Indentifying the two wetting states on the CNT-polymer nanocomposites provides a general method for studying the various liquid-solid interfaces on the nanoscale. The stable CNT-polymer nanocomposites fabricated in the present thesis can be used as an antistick coating in MEMS systems, or as a protective thin film under stressed conditions (such as long time immersion in sea water for long duration). The discovered inverse correlation between R_s and R_p contributes to the improvement of the solar cell fill factor, and thus affects power conversion efficiency, and further provides new insight into the relationship between the interfacial contacts and the performance of organic solar cells.

The energy conversion efficiency of the solution processed CuPc organic solar cells (Chapter 3.3, 3.4) is too low, due to the low light absorption efficiency in the bilayer structure. If the bulk heterojunction is employed to increase the light absorption efficiency, the energy conversion efficiency would drop to 0.06%, due to the interfacial contact problem in the construction of the nanostructure. Therefore, a well connected bulk heterojunction, becomes a critical challenge to the successful fabrication of the solar cells with high efficiency. The contact resistance of the CuPc nanoaparticles and CuPc-PCBM interface will have to be investigated. The role of charge transport across the CuPc nanoaparticle interface will also be studied by numerical modeling. To confirm the stability of the devices, various types of buffer layers will be incorporated between the organic and metal electrode layers as a preliminary measure to improve the photo-stability of the interface. Further study of the effect of the photo-degradation of the organic/metal electrode interface on other device parameters, such as the quantum efficiency, dark current and open circuit voltage will also be carried out.

Appendix: Molecular Structures

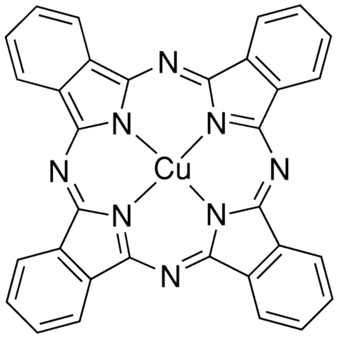

Figure 5.1: Molecular structure of copper phthalocyanine (CuPc).

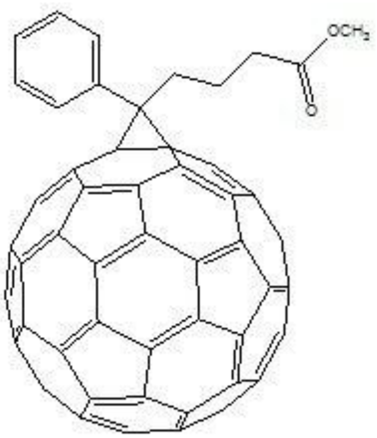

Figure 5.2: Molecular structure of [6, 6]-phenyl- C_{61}- butyric acid methyl easter (PCBM).

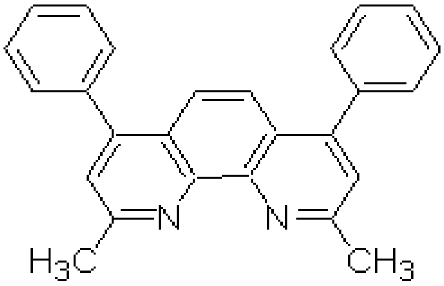

Figure 5.3: Molecular structure of bathocuproine (BCP).

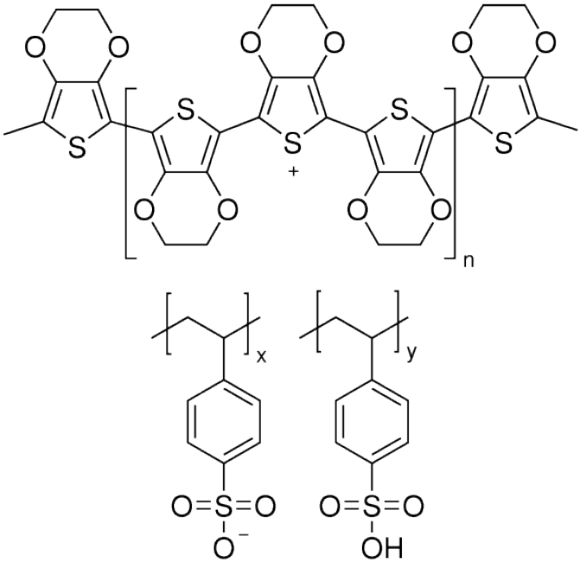

Figure 5.4: Molecular structure of Poly (3,4-ethylenedioxythiophene)- poly (styrenesulfonate) (PEDOT:PSS).

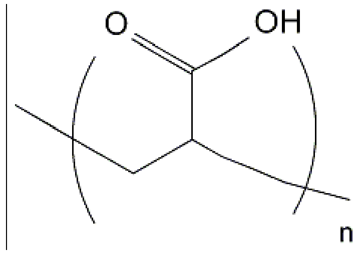

Figure 5.5: Molecular structure of Poly (acrylic acid) (PAA).

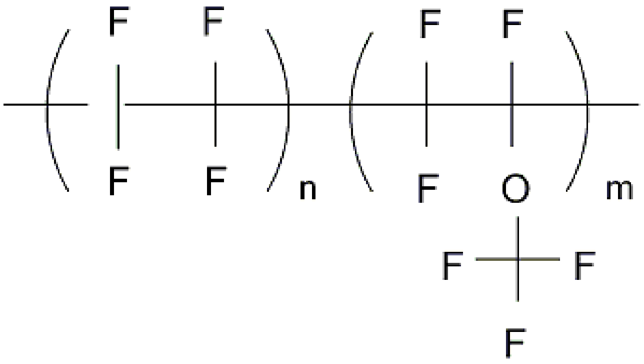

Figure 5.6 Molecular structure of perfluoroalkoxy copolymer resin (PFA).